2021

# Characteristics of excitatory synapses and mutant huntingtin distribution in the Q175 mouse model of Huntington’s disease

BOSTON UNIVERSITY
SCHOOL OF MEDICINE

Thesis

# CHARACTERISTICS OF EXCITATORY SYNAPSES AND MUTANT HUNTINGTIN DISTRIBUTION IN THE Q175 MOUSE MODEL OF HUNTINGTON'S DISEASE

by

**DICKSON TIK SANG CHEN**

B.S. University of California Los Angeles, 2019

Submitted in partial fulfillment of the

requirements for the degree of

Master of Science

2021

Approved by

First Reader _____

Jennifer I. Luebke, Ph.D.
Waterhouse Professor and Chair of Anatomy and Neurobiology

Second Reader _____

Maria L. A. Medalla, Ph.D.
Assistant Professor of Anatomy and Neurobiology

## ACKNOWLEDGEMENTS

This document is a product of my research in the Department of Anatomy & Neurobiology at Boston University School of Medicine. All the experiments and work for this project began at the start of early Spring 2020 at the very start of the COVID-19 pandemic. The pandemic proved to be a difficult time for many, with imposed limitations of in-person lab work and personal hardships. However, this work is a powerful representation of what teamwork, collaboration and persistence can accomplish and would not have been possible without my support system.

From Seattle, I would like to thank my parents, my brother Anderson, and my partner Alyssa. Thank you all for your unconditional support in my journey through medicine and the biomedical sciences. I would also like to express my tremendous gratitude to Mr. Bill Gates, Mrs. Melinda Gates, and the Bill & Melinda Gates Foundation for their generous contribution to cover the cost of my education in the master's program. From Los Angeles, I would like to thank the following members of the Levine-Cepeda lab at the University of California, Los Angeles: my PIs Drs. Michael Levine and Carlos Cepeda, my lab partner Vannah, and Drs. Sandra Holley, Joshua Barry, and Katerina Oikonomou. Without them, I would not be the scientist I am today. Thank you all for nurturing my interest of neuroscience. I would also like to recognize Mireya from the Gates Millennium Scholarship Program for helping me in the transition from undergraduate to graduate education. From Boston, I would like to thank my roommate Omar, my friends Morgane and Vibhav, my advisor Dr. Linda Afifi, my former mentor Rakin, and members

of the Luebke and Medalla Labs. My gratifying lab experience was thanks to all of these driven and amazing individuals: Afroze, Alexa, Bing, Chantal, Chrome, Diego, Dhruba, Emma, Lazaro, Louis, Mitali, Paola, Sara, Wayne, and Yuxin. It has been humbling working with you all.

Finally, I would like to express my most sincere appreciation to my research mentors. To Dr. Maria Medalla: Thank you for teaching me the complex nuances of neuroscience methods and your willingness to talk "science" with me. I am specifically grateful for a conversation we had about mHTT propagation and co-localization that led to my first IHC. I will remember the amazing things I've learned, and also the not-so-amazing times when I made mistakes. Your passion and interest for neuroscience is unrivaled and I am grateful to have worked with you. To Dr. Jennifer Luebke: Thank you for taking me on as one of your graduate students. Working in your lab has been one of the most enriching and rewarding experiences of my life. You are the most supportive and thoughtful mentor and friend I could have ever asked for. Thank you for the career advice and for constantly pushing me to be better. I will never forget the lessons you taught me on how to conduct myself as a person, professional, and scientist. In addition to being an amazing PI, scientist, and department chair, thank you fostering an inviting and collaborative lab environment and for pushing the field of neuroscience to new horizons. Your dedication and hard work is so appreciated and does not go unnoticed.

**CHARACTERISTICS OF EXCITATORY SYNAPSES AND MUTANT HUNTINGTIN DISTRIBUTION IN THE Q175 MOUSE MODEL OF HUNTINGTON'S DISEASE**

DICKSON TIK SANG CHEN

ABSTRACT

Huntington's disease is an inherited neurodegenerative disease characterized by the degeneration of the cerebral cortex, thalamus, and striatum. The loss of neurons in the cerebral cortex and the thalamus may affect the synaptic circuitry in the striatum as these regions send glutamatergic projections (corticospinal & thalamostriatal) to neurons in the striatum. Prior studies have suggested the detrimental impact that the mutant Huntingtin protein (mHTT) may have on corticostriatal afferents, but less is known thalamic inputs to the dorsal striatum. In this study, we report a 50% reduction in thalamostriatal axospinous synapse density and significant reductions in dendritic spine volume at the ultrastructural level using electron microscopy. Additionally, dystrophic alterations to mitochondria size and morphology were also found. At the microcircuit level, we report a reduction in the spatial abundance of thalamostriatal axon terminals at the rostral, middle, and caudal levels of the dorsolateral striatum while an inverse distribution was observed for mHTT, suggesting a novel topographic distribution of thalamostriatal projections and mHTT along the rostral-caudal axis of the dorsolateral striatum. These findings are novel in the $Q175^{+/-}$ HD mouse model and supports the theory of an excitatory: inhibitory imbalance contributing to structural synaptic changes in the dorsal striatum. Further studies of the corticostriatal projections will determine the global extent of this imbalance.

TABLE OF CONTENTS

ACKNOWLEDGEMENTS …….. iv

ABSTRACT ……..…….…... vi

TABLE OF CONTENTS …….....…… vii

LIST OF TABLES …… x

LIST OF FIGURES ……..…….. xi

LIST OF ABBREVIATIONS ……..... xii

INTRODUCTION …….. 1

Background & Prevalence of Huntington's Disease (HD) …… 1

Etiology & Pathology of HD ……..... 2

The Degenerating HD Brain ……..... 3

Function & Role of the Basal Ganglia ……...… 7

Striatal Medium-sized Spiny Neuron (MSN) Subtypes ……..…..... 7

Direct & Indirect Pathways of the Basal Ganglia …….…… 10

Transgenic HD Mouse Models ……..... 13

Structural Alterations to MSNs in HD ……..…...…..... 16

Corticostriatal & Thalamostriatal Inputs to MSNs ……..……..…..... 18

Abnormal Mitochondria Function & Morphology in HD ……..….. 20

Purpose of the Current Study …….. 20

METHODS ……..……..... 19

Experimental Subjects ……... 22

Electron Microscopy Studies of Excitatory Axospinous Synapses ……..... 22

Perfusion & Tissue Harvesting …… 22

Pre-Embedding Labeling of VGLUT2 ……..…..... 23

Tissue Processing & Embedding for Serial Block Face Imaging …… 24

Serial Block Face 3D Electron Microscopy ……..… 25

Synapse Characterization & 3D EM Reconstructions ……..…..... 26

Confocal Microscopy Studies of Thalamostriatal Afferents ……...…...…… 27

Selection of Regions of Interest ……....……... 27

Immunofluorescence Labeling of VGLUT2 & mHTT……..... 29

Tissue Imaging with Confocal Laser Scanning Microscopy ……...…… 30

Particle & Colocalization Analyses in ImageJ ……..... 31

Statistical Analyses ……...…….. 32

RESULTS …… 35

3D EM Reconstructions of VGLUT2+ & VGLUT2- Synapses …...…….. 34

Characterization of VGLUT2+ & VGLUT2- Synapses …… 39

Comparison of VGLUT2+ & VGLUT2- Synapse Size ……..… 44

Distribution of VGLUT2+ & VGLUT2- Synapse Size ……..…..... 46

Density of VGLUT2+ & VGLUT2- Synapses …….. 50

Relationships Between Pre- & Post-Synaptic Elements ……...……...… 53

Relationship Between Group Characteristics & Ultrastructural Features …….. 55

Group Differences in VGLUT2 Particle Size ……..…….. 60

Regional Differences in VGLUT2, mHTT & Colocalized Particle Density ..... 64

DISCUSSION …….. 69

REFERENCES …… 79

CURRICULUM VITAE …….. 94

## LIST OF TABLES

Table 1: Means (± SEM) of VGLUT2+ & VGLUT2- ultrastructural features …….. 40

Table 2: Means (± SEM) of VGLUT2+ & VGLUT2- synapse densities …… 51

Table 3: ANOVA output tables for Genotype x VGLUT2 Marker ……..… 58

Table 4: ANOVA output tables for Genotype x Mitochondria Morphology …….. 59

## LIST OF FIGURES

Figure 1: Coronal slices from normal & HD human brain …… 5

Figure 2: Axial T1/T2 weighted MRI scans from normal & HD human brain ……..… 6

Figure 3: Dopamine acts differentially on D1 & D2 receptors on MSNs …...…….. 9

Figure 4: The direct and indirect motor pathways of the basal ganglia …….…….. 12

Figure 5: Regions of interest in the mouse striatum as seen on coronal sections …… 28

Figure 6: EM micrograph of VGLUT2+ & VGLUT2- axon terminals ……... 37

Figure 7: 3D model of reconstructed axospinous synapses …….……...… 38

Figure 8: Morphology & targets of VGLUT2+ and VGLUT2- boutons …… 41

Figure 9: Ultrastructural features of mitochondria …….. 43

Figure 10: Comparison of VGLUT2+ & VGLUT2- synapse size …….. 45

Figure 11: Distribution of VGLUT2+ ultrastructural features ……..….. 48

Figure 12: Distribution of VGLUT2- ultrastructural features …… 49

Figure 13: Density of VGLUT2+ & VGLUT2- synapses ……... 52

Figure 14: Linear regressions of VGLUT2+ & VGLUT2- ultrastructural features …… 54

Figure 15: Wildtype striatal neuropil immunostained for VGLUT2 ……... 61

Figure 16: Q175 striatal neuropil immunostained for VGLUT2 …… 62

Figure 17: Distribution of VGLUT2+ particle size ……...….. 63

Figure 18: Q175 striatal neuropil immunostained for mHTT ……..……... 66

Figure 19: Q175 striatal neuropil immunostained for VGLUT2 & mHTT …… 67

Figure 20: Distribution of VGLUT2, mHTT & colocalized particles …… 68

## LIST OF ABBREVIATIONS

D1 MSNs …… MSNs expressing D1 receptors

D2 MSNs …… MSNs expressing D2 receptors

DA ……...…… Dopamine

DAB …….. 3'-diaminobenzine

ENK ……..….. Enkephalin

EM ……. Electron Microscopy

GABA ……..…… $\gamma$- aminobutyric acid

GPe …….. Globus Pallidus, External Segment

GPi ……... Globus Pallidus, Internal Segment

HD ……. Huntington's disease

HTT …… Huntingtin Protein

mHTT …… Mutant Huntingtin Protein

MSN ……..…… Medium-sized Spiny Neuron

NA ……...…… Nucleus Accumbens

PolyQ ……... Polyglutamine

SNc …….. Substantia Nigra Pars Compacta

SNr ……. Substantia Nigra Pars Reticula

SP ……..…… Substance P

STN …… Subthalamic Nucleus

VA/VL …….. Ventral Anterior & Lateral Thalamic Nuclei

VGLUT1 / 2 ……...…… Vesicular Glutamate Transporters 1 / 2

# INTRODUCTION

## *Background & Prevalence of Huntington's Disease (HD)*

In today's era of medical mysteries, neurodegenerative diseases have risen to the forefront of modern scientific investigation and research. As one of many disorders that have no known cure, Huntington's disease (HD) stands out as a notable genetic neurodegenerative disease with debilitating symptoms. HD is a hyperkinetic movement disorder that leads to the progressive deterioration of motor, cognitive, and psychiatric faculties (Harper & Jones, 2002). A distinct hallmark of HD is the early prevalence of choreiform movement, a motor dysfunction characterized as uncontrollable dance-like movements (NINDS, 1998), and subsequently other motor deficits such as rigidity and impaired coordination. Cognitive deficits such as inability to multitask and perform executive function tasks (Papoutsi, Labuschagne, Tabrizi, & Stout, 2014), have also been reported. Onset of HD has been shown to result in the progressive manifestation of neuropsychiatric symptoms such as apathy, irritability, and depression (Craufurd et al., 2001).

Around 5.70 per 100,000 people are affected by HD in North America, Europe, and Australia (Pringsheim et al., 2012), with a prevalence of 6.52 per 100,000 people in the United States (Bruzelius et al., 2019) alone. Those with HD develop symptoms that progressively impact activities of daily living. After initial diagnosis, adult HD patients on average typically live for an additional 10-20 years. In less than 10% of reported HD cases, a juvenile form of the disease (JHD) affects children and adolescents (Huntington's Disease Society of America) with typically adult-onset symptoms manifesting *prior* to

adulthood. The life expectancy of children with this phenotype is notably shorter. Both forms of HD have no cure and limited treatment options, emphasizing the importance of conducting scientific and clinical research to prolong life and improve the quality of life of HD patients.

***Etiology & Pathology of HD***

HD is an autosomal dominant inherited disease. Patients with HD carry a mutated heterozygous copy of *huntingtin* (one normal allele, one mutated allele), a gene that encodes the production of the huntingtin protein (HTT). The mutation, which can be traced to the 4p16.3 gene, is characterized by the unstable expansion of glutamine (CAG) trinucleotide repeats within exon 1 (HDCRG, 1993). The normal *huntingtin* gene (*HTT*) contains 6-34 CAG repeats. In patients with HD, *HTT* contains a polyglutamine (polyQ) sequence attached to the $NH_2$ terminal that exceeds 35 repeats (HDCRG, 1993). The length of the expanded *HTT* polyQ sequence has previously been shown to result in abnormal splicing of *HTT* mRNA (Sathasivam et al., 2013) and alterations to normal post-translational modifications involved with HTT cleavage (Graham et al., 2006). Prior research also shows an inverse correlation between the length of the polyQ expansion and age of onset when HD symptoms are first reported – longer CAG repeat expansion sequences were found to contribute to the manifestation of HD pathology at earlier ages. (Andrew et al., 1993; Swami et al., 2009). Together, these results implicate polyQ sequence length as the basis for HD, influencing phenotypic severity and producing a mutant form of the huntingtin protein (mHTT).

The production of misfolded fragmented mHTT proteins leads to protein aggregation in specific brain regions. Studies in transgenic HD model mice and in human HD brains show that mHTT aggregates appear mainly in the cerebral cortex and the striatum, localizing in striatal nuclei after the misfolded protein oligomerize and form inclusions, as well within dystrophic neurites and the cytoplasm (Davies et al., 1997; DiFligia et al., 1997; Gutekunst et al., 1999). Though the role of normal HTT is not fully understood, it is believed that the protein has regulatory functions in a variety of critical cellular processes such as gene transcription, vesicular transport, brain-derived neurotrophic factor (BDNF) production, normal synaptic functioning, neurodevelopment, and neuronal axonal transport (Cattaneo, Zuccato, & Tartari, 2005; Sugars & Rubinsztein, 2003; Zuccato & Cattaneo, 2014; Trushina et al., 2004). The production of mHTT and the formation of inclusion bodies impairs these vital cellular processes. Due to limited research, the molecular mechanisms by which mHTT disrupts these processes are unclear. Some studies suggest that mHTT aggregates alter transcriptional regulators responsible for neuronal survival (Jiang et al., 2003) and players responsible for the maintenance of the proteosome network (Bence et al., 2011).

### *The Degenerating HD Brain*

It remains a topic of controversy whether the formation of inclusion bodies is an autonomous toxic cell response, or whether it is a non-cell autonomous neuroprotective response to neuronal dysfunction and degeneration. However, one thing remains clear – the formation and aggregation of mHTT is a precursor event that leads to the pathogenesis of HD. With the progression of the disease, HD symptoms continue to worsen, and the loss

of synaptic connections are observed. Morphological studies reveal significant atrophy of neurons in HD, most notably in the striatum, but also in the neocortex and subcortical structures like the thalamus (Vonsattel & DiFiglia, 1998). These brain regions, more predominantly the cerebral cortex and the striatum, are the focus of extensive research to investigate mechanisms that contribute to region-specific degeneration. In a side-by-side comparison of coronal brain sections, drastic changes in size and structure can be seen between the normal and HD human brain (Fig. 1). In the HD brain (left), a large reduction in the cerebral cortex and the caudate nuclei of the basal ganglia can be seen in addition to enlargement of the lateral ventricles (Fig. 1). On T1 and T2 MRI images, atrophy of the caudate nuclei is evident with enlargement of the frontal horns of the lateral ventricles in the HD brain (Fig. 2). Other early studies demonstrate that the caudate and putamen nuclei are highly susceptible to degeneration. One postmortem study demonstrated a 57% reduction of caudate cross-sectional area and a 64% reduction of putamen cross-sectional area in HD brains (grades 0 – 4 on a clinical HD severity scale) when compared to controls (Monte, Vonsattel, & Richardson, 1998). To fully grasp the magnitude of these changes in the brain, an understanding of the function, motor pathways, inputs and outputs of basal ganglia structures is necessary.

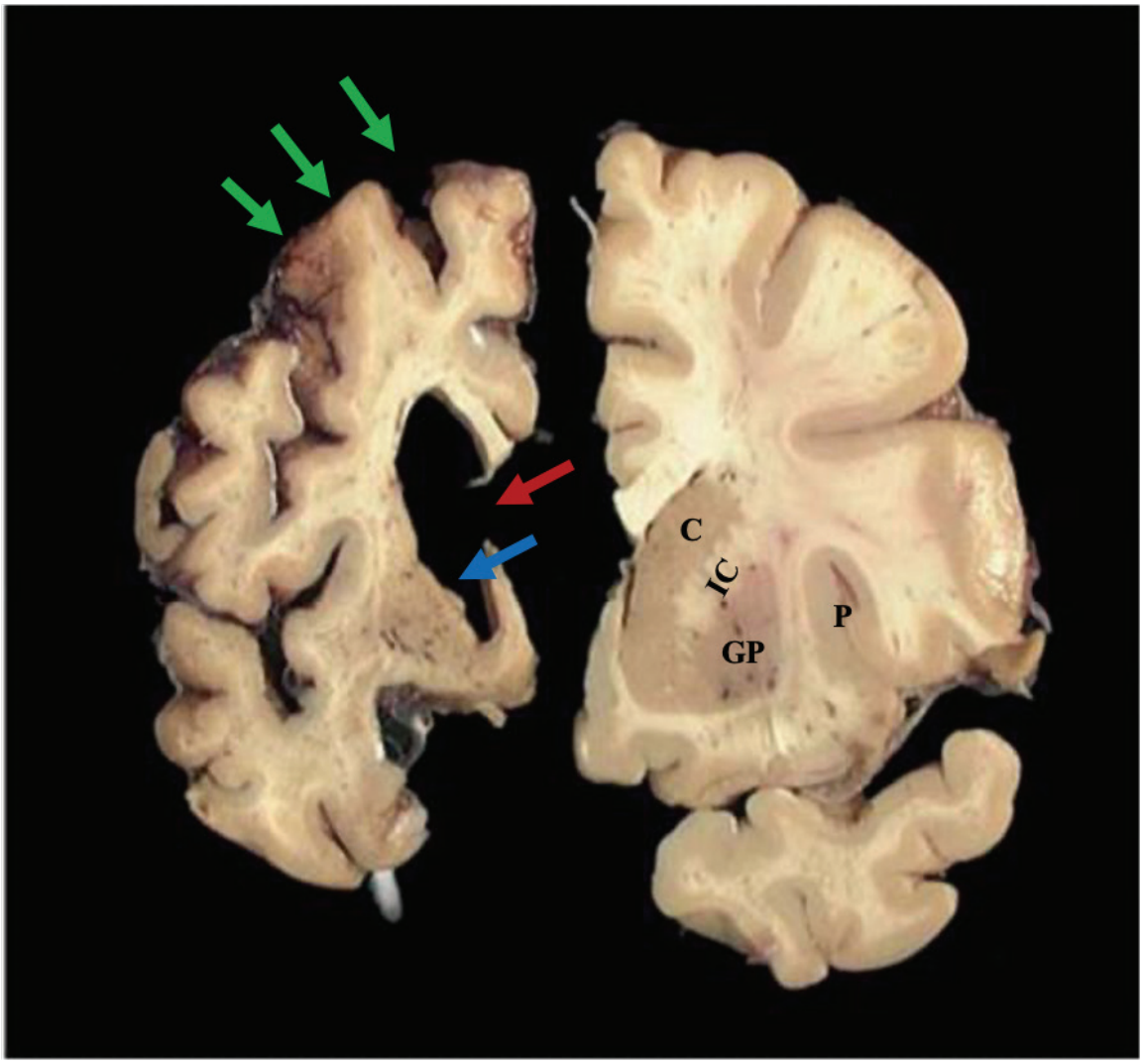


**Figure 1: Coronal slices from normal & HD human brain.** Coronal slice of the telencephalon of an advanced HD brain (grade 4) (LEFT). Coronal slice of the telencephalon of a normal brain (RIGHT). Red arrow indicates expansion of the lateral ventricles. Green arrows denote reduction in cerebral cortex volume. The blue arrow shows the reduction in caudate size. Figure adapted from Reiner, 2011. Image courtesy of the Harvard Brain Tissue Research Center. Abbreviations: C, caudate; GP, globus pallidus; P, putamen; IC, internal capsule

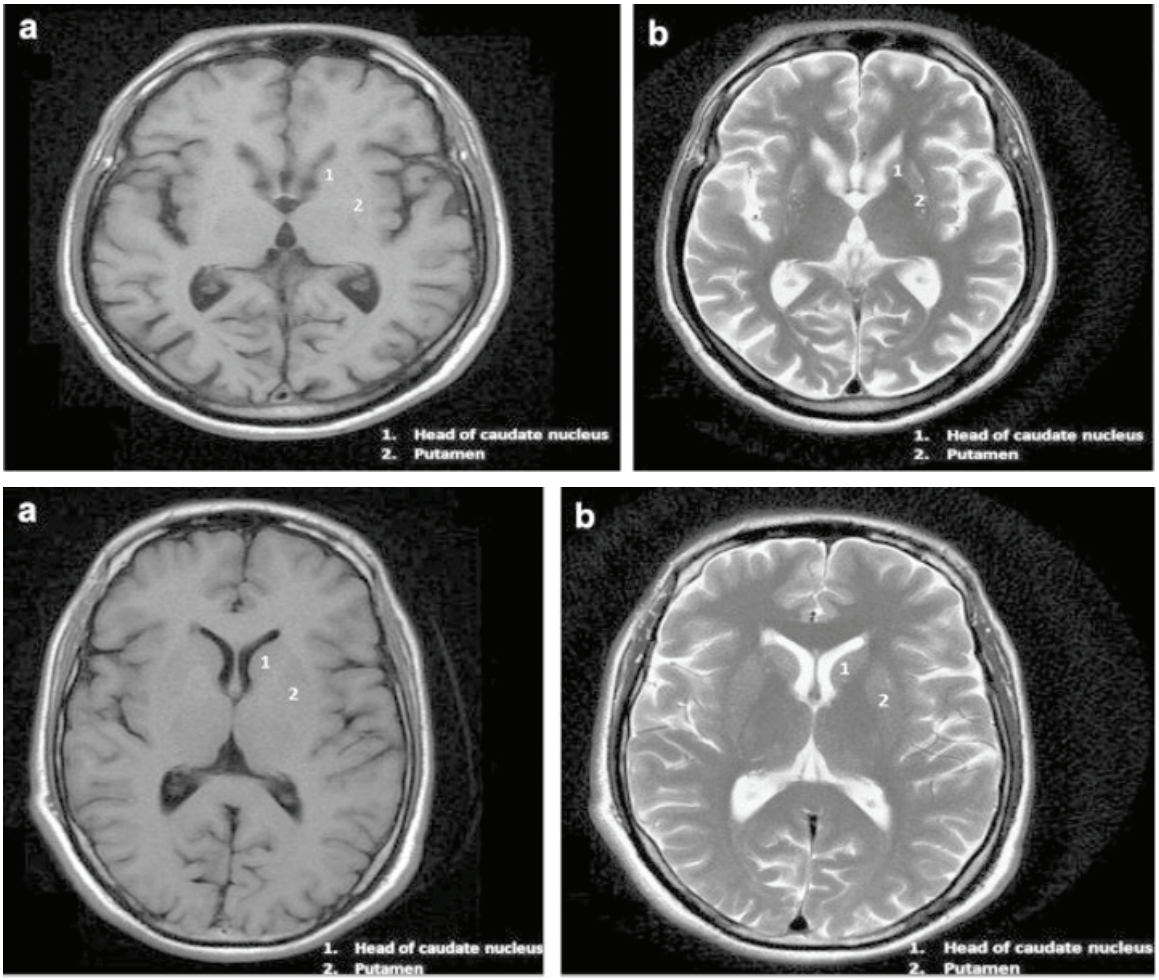


**Figure 2: Axial T1/T2 weighted MRI scans from normal & HD human brain.** T1 (a)and T2-weighted (b) scans of a middle-aged HD brain at the level of the basal ganglia (TOP). T1 (a) and T2-weighted (b) scans of a normal brain at the level of the basal ganglia (BOTTOM). Figure adapted from Negi et al., 2014. Abbreviations: 1, head of caudate nucleus; 2, putamen

### *Function & Role of the Basal Ganglia*

The basal ganglia is a structure made of a cluster of subcortical structures that consist of the dorsal striatum (caudate and putamen), ventral striatum (nucleus accumbens, or NA), globus pallidus (GPi and GPe), ventral palladium, substantia nigra (SNc and SNr) and the subthalamic nucleus (STN) (Fix, 2008). Collectively, the striatum is involved with the coordination of cognitive tasks, such as action selection and reinforcement learning (Stocco et al., 2010), as well as emotional processing tasks which are facilitated by close anatomical associations with structures of the limbic system. The dorsal striatum specifically is primarily involved with the regulation of voluntary motor control. Collectively, neurons in the caudate and putamen process reward and sensory inputs, relaying the appropriate motor commands to the decision-making cortices to ensure adequate time is given in preparation for a planned motor movement (Chakravarthy, Joseph, & Bapi, 2010). This feedforward and feedback mechanism ensures that movement is smooth and fluid. Thus, the striatum plays an important role as the "integrator," processing afferent information and regulating voluntary motor movements.

### *Striatal Medium-sized Spiny Neuron (MSN) Subtypes*

The striatum contains specialized medium-sized spiny neurons (MSNs) which make up the majority of all neurons. MSNs are projection neurons that secrete the inhibitory neurotransmitter $\gamma$-aminobutyric acid (GABA), and they process afferent information and relay feedback to other basal ganglia structures to initiate, facilitate, and execute motor movement. MSNs receive excitatory afferents from the cerebral cortex and the thalamus and relay information to other basal ganglia structures via parallel motor

circuits called the direct and indirect pathways. Appropriate efferent information is then relayed to the motor cortices to modulate motor activity. Within the motor pathways, MSNs can be divided into two subtypes based on the expression of dopamine (DA) receptors: striatonigral MSNs that express D1 receptors (D1 MSNs), and striatopallidal MSNs that express D2 receptors (D2 MSNs) (Gerfen et al., 1990). Together, these two subclasses of MSNs make up approximately 90-95% of all neurons in the striatum (Graveland & Difiglia, 1985).

The SNc, which releases DA, sends afferent projections to MSNs. DA modulates the activation of the direct and indirect pathways by acting differentially on the DA receptors of D1 and D2 MSNs, activating D1 receptors and inhibiting D2 receptors (Gerfen & Surmeier, 2011) (Fig. 3). While both D1 and D2 MSNs secrete GABA and are modulated by DA, they express different neuropeptides, namely D1 MSNs express substance P (SP), while D2 MSNs express enkephalin (ENK) (Gerfen et al., 1990). Both SP and ENK serve neuroregulatory roles, modulating the release of excitatory transmitter glutamate and ensuring neurons are not overactivated (Blomeley, Kehoe, & Bracci, 2009; Steiner & Gerfen, 1998). DA has also been reported to differentially regulate the expression of the neuropeptides in the respective MSN subtypes (Gerfen, Mcginty, & Young, 1991).

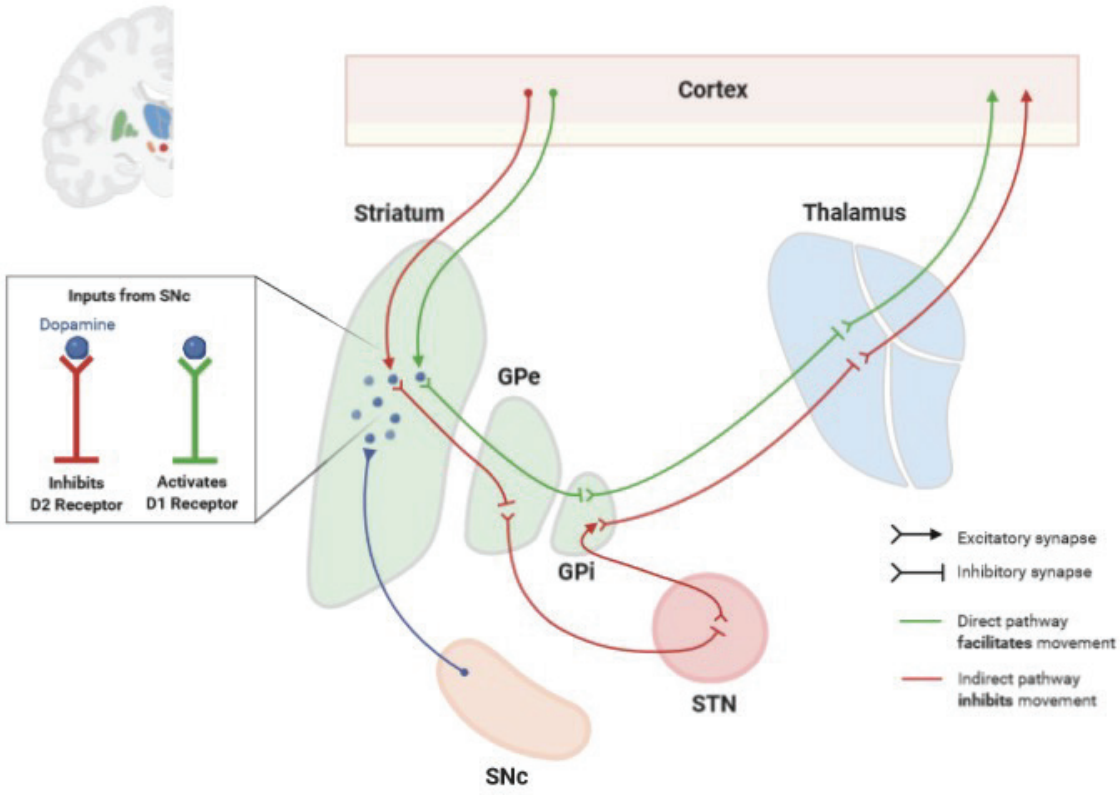


**Figure 3: Dopamine acts differentially on D1 & D2 receptors on MSNs.** The direct and indirect pathways process information from the cortex. DA from SNc modulates the activation of these pathways by differentially acting on D1 and D2 receptors of MSNs in the striatum. Figure adapted from BioRender, 2020. Abbreviations: GPe, external segment of the globus pallidus; GPi, internal segment of the globus pallidus; SNc, substantia nigra pars compacta; STN, subthalamic nucleus

### *Direct & Indirect Pathways of the Basal Ganglia*

The direct and indirect motor pathways of the basal ganglia play important roles in the modulation of motor activity. Generally, MSNs from each respective pathway receive extrinsic glutamatergic projections from the cerebral cortex and the thalamus as well as intrinsic dopaminergic projections from the SNc (Gerfen & Surmeier, 2011). The glutamatergic projections are relayed to different basal ganglia structures based on the MSN subtype, differentially modulating the activity of the MSNs in each pathway. The final basal ganglia output structures send efferent projections to thalamic and brainstem nuclei to modulate the activity of motor neurons. The structures and neurotransmitters of each pathway are summarized in Figure 4.

In the direct pathway, excitatory glutamatergic inputs from the cerebral cortex and the thalamus activate GABAergic D1 MSNs in the striatum. Neurons in the SNc secrete DA, which binds to D1 receptors, further activating D1 MSNs. Excitation of MSNs increases the secretion of GABA, causing a strong inhibitory effect on GPi neurons, which are also inhibitory in nature. Consequently, the GPi neurons secrete less GABA to the ventral anterior and ventral lateral (VA/VL) thalamic nuclei, providing a net reduction of inhibition to VA/VL within this pathway. Since the VA/VL nuclei are glutamatergic, this disinhibition from the GPi neurons allow the VA/VL nuclei to project more excitatory inputs to the frontal and premotor cortices, providing an overall net excitatory effect. As a result, the direct pathway is termed the "facilitatory" pathway, as components of this pathway collectively work to facilitate, initiate, and execute motor activity. The indirect pathway serves to balance the direct pathway, as the components of this pathway work to

inhibit motor activity overall. In this pathway, excitatory glutamatergic inputs from the cerebral cortex and thalamus activate GABAergic D2 MSNs in the striatum. Neurons in the SNc secrete DA, which binds to D2 receptors. However, instead of providing an excitatory effect as seen in the direct pathway, DA serves a different role, inhibiting D2 MSN activation and dampening excitation. As a result, D2 MSNs secrete less GABA and provide weaker inhibition of neurons in the GPe which are also inhibitory in nature. Consequently, GPe neurons secrete more GABA to the STN, causing the STN to project more excitatory glutamatergic inputs to GPi neurons. This is where the indirect pathway converges with the direct pathway. Due to increased excitation from the STN, the inhibitory GPi neurons then secrete increased levels of GABA onto the VA/VL thalamic nuclei, causing VA/VL to project less excitatory inputs to the frontal and premotor cortices, producing an overall net inhibitory effect. As a result, the indirect pathway is termed the "inhibitory" pathway, as the components of this pathway work to limit motor activity.

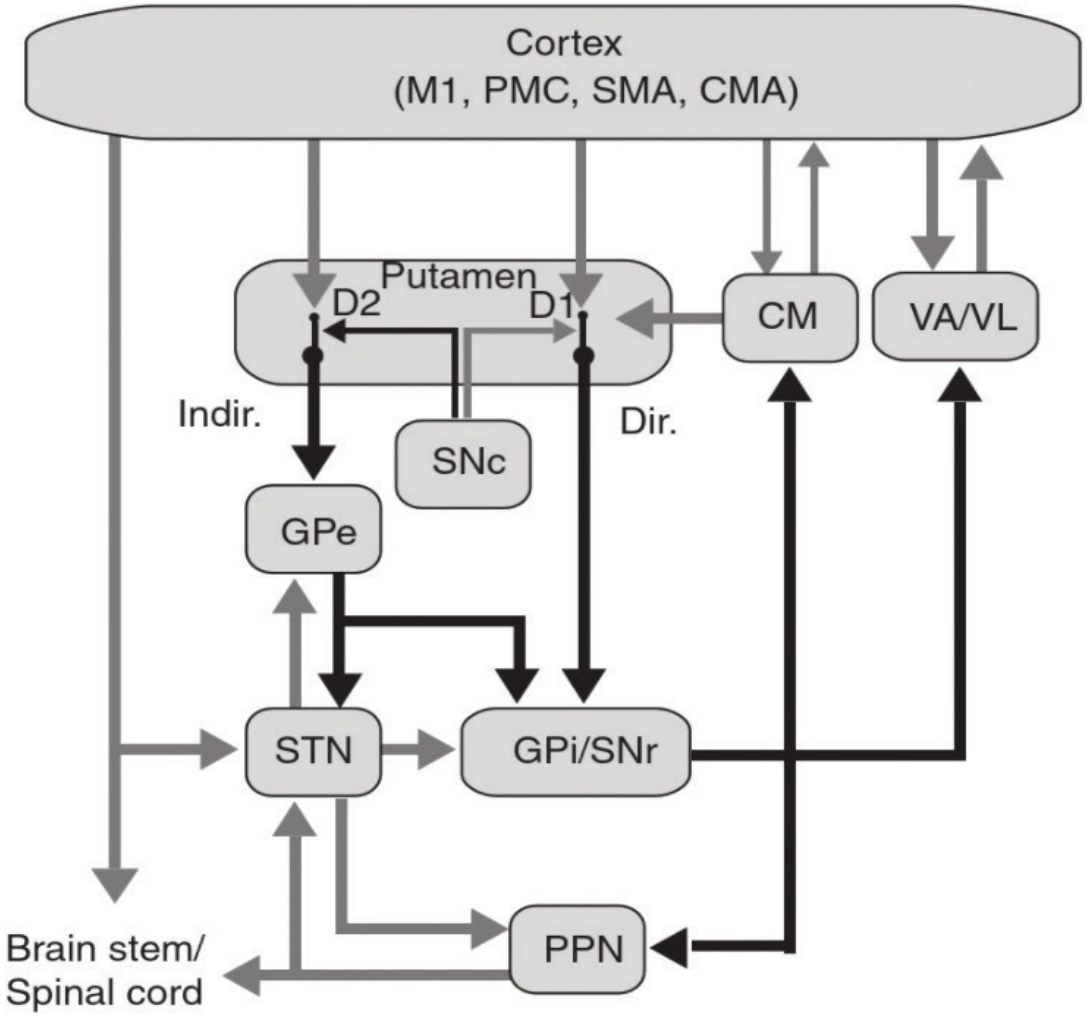


**Figure 4: The direct and indirect motor pathways of the basal ganglia.** MSNs receive excitatory afferents from numerous cortical areas (M1, PMC, SMA, CMA), the thalamus (CM) and the SNc from within the basal ganglia. Efferent outputs from the GPi and SNr are projected onto thalamic (VA/VL) and brainstem nuclei (PPN) to modulate motor neuron activity in the brain stem/spinal cord and the motor cortex. Black arrows indicate inhibitory projections. Gray arrows indicate excitatory projections. Figure adapted from Galvan, 2014. Abbreviations: CM, centromedian nucleus of the thalamus; CMA, cingulate motor area; Dir., direct pathway; GPe, globus pallidus, external segment; GPi, globus pallidus, internal segment; Indir., indirect pathway; M1, primary motor cortex; PMC, pre-motor cortex; PPN, pedunculopontine nucleus; SMA, supplementary motor area; SNc, substantia nigra pars compacta; STN, subthalamic nucleus; VA/VL, ventral anterior/ventral lateral nuclei of the thalamus

Knowledge of the parallel motor pathways reiterate the opposing, yet important roles of D1 and D2 MSNs in modulating motor activity. In line with findings of degenerating MSNs in the caudate and putamen of HD patients, an imaging study examining dopamine receptor binding demonstrates that both D1 and D2 dopamine receptors in the caudate and putamen are lost as well in symptomatic and asymptomatic HD patients (Weeks et al., 1996). In the scope of the indirect pathway, the atrophy of D2 MSNs results in less inhibitory projections to the GPe. Consequently, GPe neurons would have a larger inhibitory control over the STN with the secretion of more GABA onto neurons in the GPi. This leads to an overall disinhibition of the thalamus as GPi neurons secrete less GABA onto the thalamic nuclei, contributing to increased thalamic excitation. Overall, the loss of MSNs in HD generates a net excitatory effect in the indirect pathway.

***Transgenic HD Mouse Models***

The degeneration of MSNs within the striatum highlights the importance of developing effective models to study HD. Over time, transgenic mouse models have been developed and refined to study the neuropathological, functional, and morphological changes that mimic those seen during HD progression. Using mouse models to study HD provides benefits as these tools allow for visual and quantitiatve assessments of changes to vulnerable brain regions such as the striatum and cerebral cortex during stages of progression. While all models have contributed to novel discoveries, each HD model varies based on its genetic makeup and the way they were genetically engineered. The first widely used transgenic models for studying HD were the R6/1 and R6/2 mouse models. These models are fragment models and created by introducing a plasmid that contain a small N-

terminus fragment of the mutant human HD gene, including the promoter sequences, exon 1, and the polyQ sequence. R6/1 and R6/2 mice contain polyQ sequences with 116 and 144 CAG repeats respectively (Mangiarini et al., 1996). Though the R6/2 mouse model has been widely used in behavioral studies, due to the way the plasmid was genetically introduced, the length of polyQ repeats is unstable and may vary within the germ and somatic lines (Bates, 1997). Another study found that R6/2 mice with 110 and 160 polyQ repeats had a greater density of mHTT inclusions and aggregates at earlier ages compared to mice with 210 and 310 polyQ repeats (Cummings et al., 2012). This finding contradicts the relationship observed in humans where longer polyQ lengths are associated with earlier disease severity (HDCRG, 1993). Together, these findings suggest that the R6/2 model may not be the best model to study the time-sensitive neuropathological changes observed in human HD progression.

Unlike R6/1 and R6/2 fragment models, full length mouse models such as YAC128 and BACHD mice are genetically engineered using a full-length copy of the mutant gene. To generate YAC128 mice, plasmids containing multiple full-length copies of mutant human *HTT* (116 CAG and 9 CAA polyQ repeats) are introduced into mice via a yeast artificial chromosome while BACHD mice are formed by the introduction of a plasmid containing full-length copies of the mutated human HTT (97 CAG-CAA polyQ repeats) via a bacterial artificial chromosome (Pouladi et al., 2012; Gray et al., 2008). Though no evidence of somatic instability has been reported in these full-length models, a study showed differences between the mouse models where accumulation and spread of mHTT aggregates was present in the YAC128, but absent in the BACHD model (Pouladi et al.,

2012). The same study also found decreased mRNA gene expression in the striatum for the YAC128 model, but no changes to the BACHD model. These differences could be attributed to the presence of a mixed glutamine polyQ sequence (CAG and CAA) instead of a pure CAG sequence (Pouladi et al., 2012). These findings suggest that using YAC128 or BACHD mice for mHTT histological studies may not be ideal as the mixed CAG-CAA polyQ repeats may serve as a confounding factor. Additionally, what is observed from these histological studies may not be an accurate representation of what is happening in the human HD brain since pathophysiology is caused by pure CAG polyQ expansion of *HTT*, not mixed.

Of all rodent models, knock-in models are by far the most realistic rodent models of human HD are. Unlike the fragment and full-length models which introduce a foreign plasmid into the mouse genome, knock-in mice are generated using mouse embryonic stem cells with a pre-determined polyQ repeat length. By using homologous recombination, a chimeric mouse-human exon 1 with pure CAG polyQ repeats can be created within the native full-length mouse *HTT* locus, preventing issues of somatic instability. Additionally, these transgenic mice are heterozygous, with one normal allele and one mutated *HTT* allele, mirroring the genetic etiology seen in HD patients. The two commonly used knock-in models are the CAG140 (referred to as Q140) and the zQ175 (referred to as $Q175^{+/-}$) mice which contain 140 and 188 CAG polyQ repeats within their *HTT* gene respectively (Menalled et al., 2012). Aside from the longer polyQ length, the $Q175^{+/-}$ model is identical in genetic construction to the Q140 mouse model. Based on motor assessments and

neuropathological findings, both models are useful to studying mechanisms underlying neuronal dysfunction (Menalled, Sison, Dragatsis, Zeitlin, & Chesselet, 2003; Menalled et al., 2012). Of all discussed transgenic rodent models, the Q140 and Q175$^{+/-}$ mouse models offer the best construct validity and may be the most accurate way to replicate human HD pathology in mice.

***Structural Alterations to MSNs in HD***

As discussed, striatal MSNs receive extrinsic glutamatergic afferents from the cerebral cortex and the thalamus in addition to intrinsic dopaminergic afferents from the SNc which modulate the activity of the direct and indirect pathways. The significant loss of MSNs during the course of HD has prompted an in-depth examination of dopaminergic projections to determine the subsequent changes to DA neuromodulation in the direct and indirect pathways. Studies of D1 and D2 MSNs in HD patients shows a pattern of time-dependent degeneration, characterized by the loss of D2 (ENK) receptors during early stages of the disease (grade 0), followed by the sequential loss of D1 (SP) receptors in all other stages (grade 2, 3) of disease progression (Glass, Dragunow, & Faull, 2000). Similarly, immunohistochemical studies on human HD tissue demonstrate loss of ENK+ D2 MSNs early on (grade 0), followed by reduction (grade 1+) of SP+ D1 MSNs at a later stage of disease progression (Deng et al., 2004). These findings suggest that indirect pathway MSNs are more susceptible to degeneration at earlier timepoints than direct pathway MSNs.

The combination of findings in these studies support a pattern of selective neuronal vulnerability to degeneration based on the stage of HD progression, characterized by high

initial vulnerability of D2 MSNs during earlier stages, followed by a gradual reduction in D1 MSNs with disease progression. These observations mirror the chronology of HD symptoms, as HD patients develop involuntary choreiform movements early on in the trajectory of the disease, followed by the loss of ability to control voluntary movements, resulting in motor deficits such as incoordination and bradykinesia (Bates et al., 2014). Initial choreiform symptoms may be attributed to the early susceptibility of D2 MSNs to degeneration, while loss of voluntary motor control can be due to further degeneration of both D2 MSNs and D1 MSNs at later stages. These early findings suggest that MSN loss may result in differential changes to striatal microcircuitry.

Elucidating the specific mechanisms responsible for alterations to synaptic connections in the striatum requires in-depth characterization of the structural properties of MSNs. In four different studies, quantifications of dendritic spine density paint a clear picture of the structural changes to MSNs. Studies in symptomatic (3-month-old) R6/2 mice demonstrate reduced dendritic spine density on MSNs (Klapstein et al., 2001). In aged (18–23-month-old) BACHD mice, a 35% reduction in dendritic spine density on MSNs was observed (Rocher et al., 2016). At 7 and 12 months, both homozygous and heterozygous Q175 mice also show reduced dendritic spine density on MSNs (Indersmitten, Tran, Cepeda, & Levine, 2015). While these studies are in clear agreement of degenerative changes to dendritic spines at the symptomatic stage, it is unclear whether these observations are observed among D1 and D2 MSNs. From our lab, a recent study found that the density of D1 dendritic spines on MSNs was significantly decreased at 12 months in heterozygous $Q175^{+/-}$ mice while no changes were observed for D2 spine density

(Goodliffe et al., 2018). All studies demonstrate that there are post-synaptic structural changes to MSNs in the HD models. Electrophysiological assessments in the same studies also demonstrate functional physiological changes to MSNs. Collectively, these studies suggest that the presence of mHTT acts on dendritic spines, leading to altered synaptic transmission.

### *Corticostriatal & Thalamostriatal Inputs to MSNs*

While the activity of striatal MSNs is modulated by DA via D1 and D2 receptors, they receive glutamatergic corticostriatal inputs from the cerebral cortex and thalamostriatal inputs from the thalamus. As discussed, while the striatum undergoes the most extensive degeneration, the cerebral cortex and thalamus also undergo atrophy. These observations suggest that the loss of synaptic connections between cortical and thalamic neurons onto MSNs may also contribute to altered synaptic transmission. Studying the synaptic mechanisms of glutamatergic projections to the striatum requires in-depth characterization of the structural properties of MSNs receiving these projections. Fortunately, the axon terminals of MSNs receiving cortical and thalamic inputs can be labelled based on the expression of two subtypes of vesicular glutamate transporter to package glutamate into synaptic vesicles: excitatory cortical neuron axon terminals express vesicular glutamate transporter 1 (VGLUT1) and excitatory sub-cortical neuron axon terminals express vesicular glutamate transporter 2 (VGLUT2) (Femeau et al., 2001; Herzog et al., 2001; Fujiyama et al., 2004). Hence, the differential expression of transporter type allows corticostriatal and thalamostriatal inputs to be labelled with VGLUT1 and VGLUT2 respectively.

Although specific labelling of axon terminals allows for the characterization of structural changes to cortical and thalamic inputs to the striatum, ultrastructural studies are limited as they are labor and time intensive. An ultrastructural study of the glutamatergic inputs in the striatum of Q140 knock-in model reveals a 15-20% reduction in VGLUT1+ axon terminals (VGLUT1+ synapses) and VGLUT2+ axon terminals (VGLUT2+ synapses) in the striatum at 12-months (Deng et al., 2013). A follow up study from the same group reveals that the spatial abundance of VGLUT1+ and VGLUT2+ synapses onto D1 spines were reduced by 63.3% and 38.1% respectively at 12-months (Deng et al., 2014). A similar study in R6/2 mice (~2 to 3 months old) demonstrate a reduction in the density of excitatory axospinous synapses onto D1 and D2 spines (Parievsky et al., 2017). However, only a significant reduction among VGLUT1+ synapses was reported. In addition to assessments of spine density in the $Q175^{+/-}$ mouse, confocal imaging studies from our lab demonstrated no changes to the density of VGLUT1+ and VGLUT2+ particles found at both axodendritic and axospinous terminals in the dorsolateral striatum compared to wildtype mice (Goodliffe et al., 2018). The differing results from these studies highlights the need for additional ultrastructural studies of corticostriatal and thalamostriatal synapses in the striatum as mechanisms at the neuronal level can provide insights to the way that the presence of mHTT may be affecting glutamate neurotransmission. These alterations would affect neighboring MSNs as well, suggesting the need to study the effect of mHTT presence at both the ultrastructural and microcircuit levels.

### *Abnormal Mitochondria Function & Morphology in HD*

While confocal studies give insight to how the presence of mHTT may affect the larger projections to MSNs, mHTT may have a greater impact at a smaller ultrastructural scale that may not be observed at the microcircuit level. Ultrastructural studies provide the unique opportunity to evaluate the effect of mHTT presence on organelles such as mitochondria within pre-synaptic axon terminals arising from cortical and thalamic inputs. Studies of the normal HTT protein demonstrates its importance in the trafficking of mitochondria in neurons via binding to the HAP1 protein (Trushina et al., 2004). In the context of HD, mHTT has been found to have a higher affinity for synaptic vesicles in R6/1 and R6/2 mice, decreasing the association of HAP1 with synaptic vesicles and as well as glutamate release via synaptic vesicles (Li et al., 2003). This finding provides evidence of the effect of mHTT on mitochondria and its secondary effect on synaptic transmission. Morphological studies of mitochondria in cellular HD mouse models show evidence of mitochondrial fission, fragmentation, and disorganized dilated cristae, in addition to reduced volume (Costa et al., 2010; Song et al., 2011). Studies in moderate-to-severe grade HD patients also demonstrate a grade-dependent decline in the number of mitochondria found in MSNs (Kim et al., 2010).

### ***Purpose of the Current Study***

The structural changes to synapses with thalamostriatal (VGLUT2+) labelled axon terminals has been understudied in the field of HD. Prior studies examining the structure of VGLUT2+ synapses have yielded conflicting results at the ultrastructural and microcircuit levels. The main goal of the current study seeks to investigate the effects of

mHTT on VGLUT2+ synapses in the knock-in Q175$^{+/-}$ mouse model compared to wildtype. The first part of this study characterizes the ultrastructural features of thalamostriatal (VGLUT2+) and non-thalamostriatal (VGLUT2-) axospinous excitatory synapses in the neuropil of the dorsal striatum using serial block-face scanning electron microscopy (EM) and 3D reconstruction techniques. Examination of synapse density, characteristics, mitochondria morphology, and distribution of synapse size will reveal insights into synaptic functioning with presence of mHTT at the single neuron level.

The second part of this study examines the density, distribution and colocalization of mHTT at immunolabeled VGLUT2+ axon terminals at three levels of resolution in the striatum along the rostral-caudal axis using a combination of immunofluorescent techniques, confocal light microscopy and particle and colocalization analyses. These studies will reveal the extent to which mHTT influences excitatory inputs to the striatum at the neuron population level. Together, the results of this study will describe the mHTT-derived changes that occur in the dorsolateral striatum at multiple levels in an important and widely used mouse model of HD. At the ultrastructural level, we expect to see differences in synapse characteristics, size, and mitochondria morphology between genotype and VGLUT2+/- groups. At the microcircuit level, we expect to see differences in VGLUT2 and mHTT density and distribution between the varying levels in the striatum.

## METHODS

### *Experimental Subjects*

To examine the ultrastructural features of excitatory axospinous synapses in the dorsal striatal neuropil, the commonly studied Q175$^{+/-}$ mouse model of HD was selected for the electron microscopy (EM) studies. A total of five one-year old male mice (n = 2 wildtype, n = 3 Q175$^{+/-}$) were used. To examine the density, distribution and colocalization of VGLUT2 and mHTT immunolabeled particles in the dorsolateral striatum, a total of six one-year old male mice (n = 3 wildtype, n = 3 Q175$^{+/-}$) were used. All mice used were obtained from the CHDI Foundation (CHDI-81008006) and were individually housed at Boston University School of Medicine (Boston, MA) at the Laboratory Animal Science Center and kept under a 12 h light/dark cycle. The Boston University School of Medicine is fully accredited by the Association for Assessment and Accreditation of Laboratory Animal Care (AAALAC). All animal care and experimentation were done with accordance to guidelines provided by the *Guide for the Care and Use of Laboratory Animals* (NIH, 2011) and the *US Public Health Service Policy on Humane Care and Use of Laboratory Animals* (OLAW, 2015).

### Electron Microscopy Studies of Excitatory Axospinous Synapses

### *Perfusion & Tissue Harvesting*

Mice were anesthetized with an intraperitoneal injection of sodium pentobarbital for thoracotomy, as described (LeBlang et al., 2020). Briefly, a Socumb Solution (6 g

Sodium Pentobarbital/250mL, Henry Schein) with a 1:5 dilution factor in sterile saline was delivered at 15 μL/2 g body weight. Animals were then perfused transcardially with a fixative solution containing 1% paraformaldehyde (PFA) and 0.2% glutaraldehyde in 0.1M phosphate buffer (PB) at pH = 7.4. Next, animals received a craniotomy; the brains were removed from the skull, and the striatum was microdissected from the brain and post-fixed in the same perfusate solution (1% PFA and 0.2% glutaraldehyde) overnight at 4°C. The striatum was cut on a vibrating microtome (Leica VT1000S) into 100 μm coronal sections.

***Pre-Embedding & Labeling of VGLUT2***

To study the ultrastructural characteristics and distribution of VGLUT2 in the striatal neuropil of the mouse dorsal striatum, tissue was labelled using immunohistochemical procedures. The 100 μm sections were incubated in 50mM glycine for 1 h to expose binding sites for antigen retrieval. Sections were then pre-blocked for 1 h in 5% normal donkey serum (NDS), 5% bovine serum albumin (BSA), and 0.025% Triton-x to further improve antigen access. Next, sections were incubated in a primary polyclonal antibody against VGLUT2 (guinea pig; 1:2000, Synaptic Systems) diluted in 1% NDS, 0.2% acetylated BSA (BSA-c, Aurion), and 0.025% Triton-x, overnight at 4°C. Tissue was microwaved in the Pelco Biowave Pro oven (Biowave; Ted Pella Inc., Redding, CA) at a low wattage (150 W for 10 min at 25°C) to assist with antibody penetration into tissue.

All sections were next incubated in a secondary biotinylated antibody (donkey anti-guinea pig IgG; Jackson ImmunoResearch) overnight at 4°C with one microwave session (150W for 10 min at 25°C). After rinsing the tissue 3 x 10 min in 0.1M PB, sections were incubated in an Avidin-Biotin-HRP solution (AB-HRP kit; Vector Elite PK-6100, Vector

Laboratories) for 1 h at 4°C. Finally, sections were incubated in a 3'-diaminobenzine (DAB) and hydrogen peroxide solution (DAB kit; Vector Laboratories) for 3 min at 25°C. Staining of the tissue with DAB initiated peroxidase-catalyzed polymerization of DAB. The immunoperoxidase reaction was terminated by washing the tissue in 0.3% $H_2O_2$ in 0.1 M PB and sections were then processed for the reaction. Following pre-embedding, tissue was rinsed in PB and post-fixed in 4% PFA and 6% glutaraldehyde in 0.1M phosphate buffer (PB) using the microwave (150-250W for 2-5 min). When the temperature of the tissue reached 30°C, the tissue was rinsed three times in 0.1 M cacodylate buffer over the duration of 1 h prior to EM processing and embedding.

***Tissue Processing & Embedding for Serial Block Face Imaging***

Tissue was processed for serial block face EM according to protocol modified from (Wang & Barbas, 2018). On day 1, sections were incubated in a solution comprised of 0.1% tannic acid in 0.1M cacodylate buffer for 30 min at room temperature (RT). Then, the tissue was osmicated in a 2% osmium tetroxide ($OsO_4$) solution containing 1.5% potassium ferricyanide (KFeCN) in 0.1M cacodylate buffer. Incubation in $OsO_4$ enables an oxidation reaction to occur in unsaturated bonds of fatty acids, adding density and contrast to tissue samples (Chissoe et al., 1995). The addition of reducing agent KFeCN with $OsO_4$ serves to enhance the contrast of membrane bound organelles such as mitochondria. After a microwave session (100W for 6 min total) and 30 min on the rotator, the tissue was incubated in 1% thiocarbohadryzide (TCH) in $dH_2O$ for 20-30 min. Next, sections were transferred to a 2% $OsO_4$ solution in $dH_2O$ and incubated using microwave assistance (100W for 6 min total), followed by 30 min in the rotator.

Tissue was then counterstained *en bloc* in 1% uranyl acetate (UA) in $dH_2O$ for 1-2.5 h. Staining with UA generated a high electron density for clear contrast visualization of cell membranes and proteins within the striatal neuropil. Sections were then submerged in a lead aspartate solution (0.04g L-aspartic acid / 10mL) for 30 min in a 60°C oven. Next, tissue was dehydrated in an ascending series of alcohols (50, 75, 85, 95% EtOH). For each series of alcohol, tissue was dehydrated for 10 minutes before the next alcohol was introduced. After dehydration, all tissue was rinsed in propylene oxide before being transferred into 20cc glass scintillation vials. Finally, all tissue was incubated in an expoxy resin solution (1:1 EM112 resin: propylene oxide) at RT for 1 h. The propylene oxide served as an intermediate solvent to aid in the transition between alcohol dehydration and the infiltration of resin into the tissue. The tissue was left overnight at RT in a dark fume hood. The next day, DMP-30 was mixed with the resin solution to accelerate resin infiltration into the tissue. After 15 minutes, tissue was transferred to a 100% accelerated epoxy resin solution for 4-6 h. Sections were then flat embedded in EM112 resin in between Aclar plastic (Ted Pella) sheets before being cured in a 60°C oven for 48-72 hrs.

***Serial Block Face 3D Electron Microscopy***

The dorsal striatum was micro-dissected from each EM112-embedded tissue to obtain blocks of embedded tissue with a 100x100 micron block face. These micro-dissected resin tissue blocks were sent to Renovo Neural (Cleveland, OH) for serial block face imaging, with similar specifications as previously described (Chen et al., 2014). All tissue was imaged using a Carl Zeiss Sigma VP scanning electron microscope equipped with a 3-View in-chamber ultramicrotome system. The microscope contained a Gatan high

sensitivity, backscattered electron detector (Gatan, England) that uses a 2.25 low-kV beam in high vacuum mode to detect images. The surface of each block of tissue embedded in resin is imaged by detecting back-scattered electrons from the tissue. Once the surface of the block was scanned, the ultramicrotome was automated to cut the block of tissue at 0.07 $\mu$m (70 nm) z-intervals. Tissue cutting and imaging was done at 6,000x magnification until serial stacks of 250-500 images of the striatal neuropil were obtained.

***Synapse Characterization & 3D EM Reconstructions***

As part of this study, a total of five datasets were examined. Each dataset belonged to a different wildtype or $Q175^{+/-}$ mouse. Aligned serial images from Renovo were analyzed using the Reconstruct™ software (http://synapses.clm.utexas.edu; Fiala et al., 2001; RRID:SCR_002716) as previously described (Medalla & Barbas, 2009). In all the datasets examined, all images had a resolution of 4.5 nm per pixel. Among all datasets, 23 fields were randomly generated and selected to be designated counting areas for synapse characterization and 3D reconstruction. Each field has a dimension of 8 x 8µm (area = 64 $\mu m^2$ / field) and spanned 3.5 $\mu$m in the z-direction. For each animal, immunolabeled VGLUT2+ and VGLUT2- axon terminals and excitatory axospinous synapses were identified and quantitatively characterized within the designated counting fields.

Axon terminals were identified based on the presence of DAB. While DAB is the main focus of this study, other chromogens such as 3,3',5,5'-Tetramethylbenzidine (TMB) and gold conjugated particles (mHTT) were used during the EM embedding and staining procedures as part of previous studies for identification of D2 receptors and mHTT respectively. On individual electron micrograph images, proteins and nucleic acids found

at DAB positive axon terminals contain a dark precipitate. Reconstructed synapses containing the dark DAB precipitate were categorized as VGLUT2+ while synapses lacking the precipitate were categorized as VGLUT2-. After DAB was identified in synaptic elements within the counting fields, object contours were generated for all elements through the entirety volume of the counting field. The presence of DAB was validated by other colleagues with extensive experience with EM reconstruction methods. All researchers were blinded to the animal's genotype during data acquisition.

## Confocal Microscopy Studies of Thalamostriatal Afferents

### *Selection of Regions of Interest*

To examine the optical density and distribution of VGLUT2 thalamostriatal axon terminals and colocalization with mHTT in the striatal neuropil, tissue sections from three levels of the striatum in each animal were selected for immunohistochemical dual labelling of VGLUT2 and mHTT. Frozen 50 μm sections were selected from a series of tissues obtained from mouse brains previously perfused with 4% paraformaldehyde. For each animal, three tissue sections were chosen based on their anatomical position within the dorsolateral striatum in the rostral to caudal direction: rostral, middle, and caudal. All slices were selected with reference to coronal Nissl sections (sections 21 to 35) of the mouse striatum as seen in the *Atlas of the Mouse Brain and Spinal Cord* (Sidman, Angevine, & Pierce, 1971). The approximate appearance and scanned area for selected rostral, middle, and caudal coronal sections are shown in similar Nissl stains shown in Figure 5.

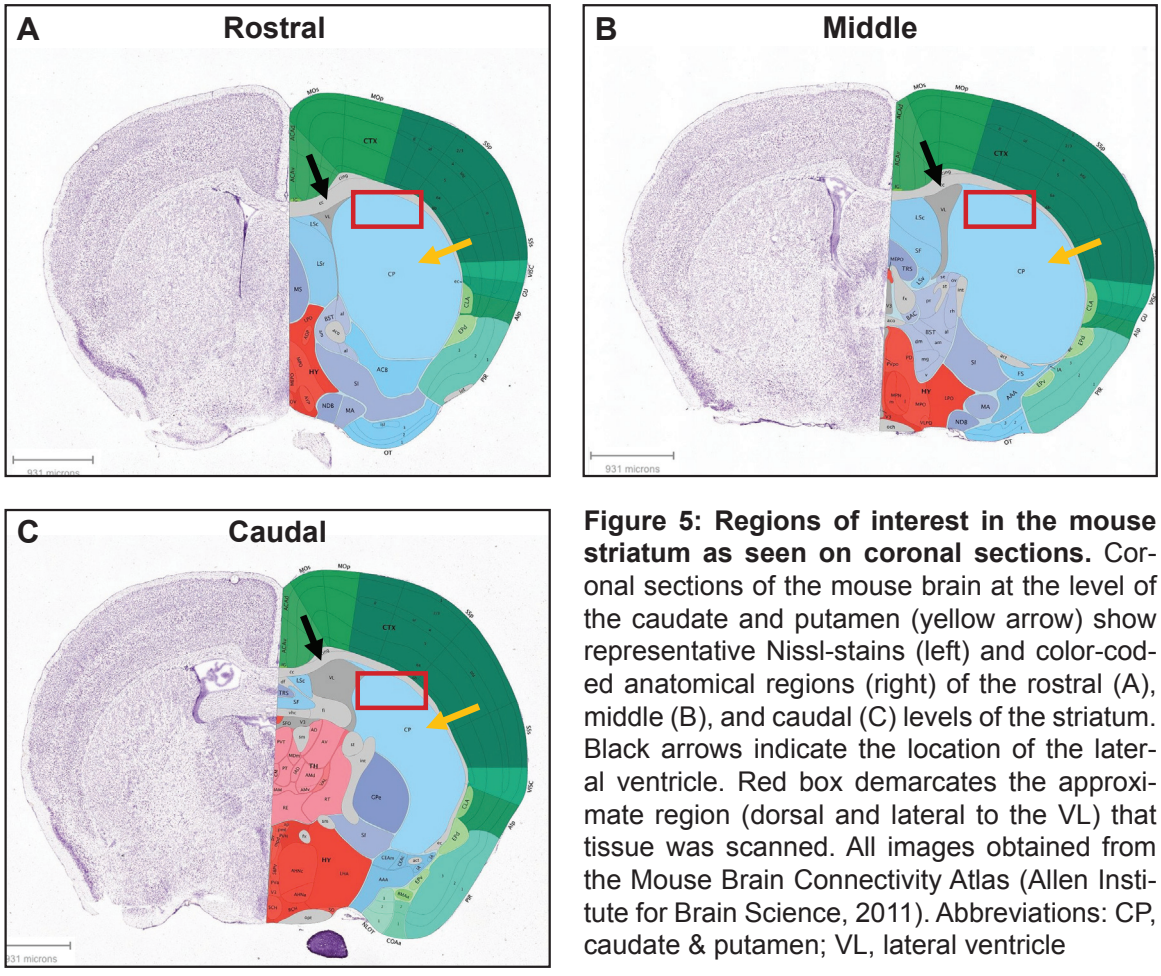


**Figure 5: Regions of interest in the mouse striatum as seen on coronal sections.** Coronal sections of the mouse brain at the level of the caudate and putamen (yellow arrow) show representative Nissl-stains (left) and color-coded anatomical regions (right) of the rostral (A), middle (B), and caudal (C) levels of the striatum. Black arrows indicate the location of the lateral ventricle. Red box demarcates the approximate region (dorsal and lateral to the VL) that tissue was scanned. All images obtained from the Mouse Brain Connectivity Atlas (Allen Institute for Brain Science, 2011). Abbreviations: CP, caudate & putamen; VL, lateral ventricle

***Immunofluorescence Labeling of mHTT & VGLUT2***

To study the density, distribution, and colocalization of VGLUT2 and mHTT within the dorsolateral striatum from the rostral to caudal direction, selected tissue was processed using immunohistochemical procedures. 50 μm sections were incubated in 50mM glycine and then placed in a water bath at 50-60°C for 1 h to unmask antigen binding sites for retrieval. Sections were then pre-blocked for 1 h in 0.01M PBS (ph = 7.4-7.5), 5% normal donkey serum (NDS), 5% bovine serum albumin (BSA), and 0.025% Triton-x to further improve antigen access. Next, sections were incubated in an antibody incubation buffer containing 0.1M PB (no saline), 0.2% acetylated BSA, 1% NDS (Vector/Jackson Labs), 0.1% Trixon-X along with primary monoclonal antibodies against VGLUT2 (guinea pig; 1:1000) and mHTT (mouse anti-EM48; 1:500). Tissue was then microwaved in the Pelco Biowave Pro oven (Biowave; Ted Pella Inc., Redding, CA) at a low wattage (2x at 150 W for 10 min at 40°C) and left to incubate overnight at 4°C. The next day, tissue was washed and then incubated in the same antibody incubation buffer with fluorescent secondary antibodies against VGLUT2 (donkey anti-guinea-pig 647; 1:200) and mHTT (donkey anti-goat 488, 1:200) primary antibodies. After the tissue incubated overnight at 4°C, all sections were mounted, and cover slipped onto glass slides with Prolong Anti-Fade (Life Technologies P36930) and left to cure in the dark at room temperature for 48-72 hrs.

### *Tissue Imaging with Confocal Laser Scanning Microscopy*

For confocal microscope analyses, tissue was imaged using a Leica TCS SPE high-resolution optical microscope. Since images from confocal microscope analyses were not used for reconstructions, tile scans were done to ensure a wide field of the dorsolateral striatum was imaged. All tiles were stitched together using the auto-stitching tool in Leica Microsystem's LAS X scanning software, creating a single continuous image with dimensions of 4 x 2 tiles. All images were scanned using a 40x objective in an oil immersion medium, with a voxel size of 0.13434 x 0.13434 x 0.5 $\mu$m and a 1.3 numerical aperture. Positions were marked in the software to denote the region of the dorsolateral striatum that was scanned. After a 4 x 2 tile area was demarcated in the dorsolateral direction relative to the lateral ventricle, the gain, offset, and z-compensation settings were adjusted for each laser channel to ensure that fluorescence was visible throughout the entire volume of each tissue section. The scanning resolution for each tile was set to 2048 x 2048 pixels. Each scan took around 1 hour to complete. All scanned images were exported into Autoquant X3 software for deconvolution. Images from two channels (546, 647) were deconvolved separately to removes optical distortions to the images caused by light scattering and other sources of noise that were present during tissue imaging. After the image quality was improved, all files were exported as 8-bit TIFF files. Images were then imported to ImageJ for particle and colocalization analyses.

***Particle & Colocalization Analyses in ImageJ***

Each 8-bit TIFF file contained a confocal stack that spanned the length of 40-60 $\mu$m. To ensure an equal volume of tissue was examined across all tissue sections, all channels in the confocal stack were merged and sub-stacked from the middle to create a 20 $\mu$m RBG stack in ImageJ. For each image in the sub-stack, an ROI detector ImageJ macro was used. First, a large general ROI of the dorsolateral striatum was manually drawn to narrow down the area for analyses to be performed. Then, five ROIs with the dimensions of 67 $\mu$m x 67 $\mu$m (500 x 500 pixels) were randomly generated by the macro within the manually generated ROI. The randomly placed ROIs were saved and imported for particle analysis and colocalization. Next, another ImageJ macro was used for quantification and colocalization analyses. For each tissue section, the minimum threshold value for immunolabeled particle detection was manually set for each channel. The "RenyiEntropy" automated thresholding method was used to assist with setting the threshold value. Before channel thresholds were set for particle analysis, the automated threshold was tested to see if particles were detected and adjusted if necessary.

After thresholds for particle detection were set for each channel, the optical density of mHTT+ and VGLUT2+ immunolabelled particles were determined in separate particle analyses within each of the five randomly placed ROIs using the particle analysis plugin in ImageJ (RRID:SCR_003070; Schneider et al., 2012). For each section, only particles with intensity values above the set threshold were quantified. Quantitative measurements such as particle count, total area, average size, and fractional area of all particles were generated for each ROI through the entirety of the 20 $\mu$m confocal stack. The optical

density of particles with overlapping mHTT+ and VGLUT2+ immunolabel were quantified in the same way using the EzColocalization plugin (Stauffer et al., 2018). All data was exported as .csv files to MATLAB.

***Statistical Analyses***

From EM studies, quantitative area and volumetric ultrastructural features of 3D reconstructed pre- and post-synaptic elements were categorized based on three categorical variables. The two main variables were: genotype (wildtype or $Q175^{+/-}$), and VGLUT2 marker (based on the presence or absence of DAB in the axon terminal, denoted by VGLUT2+ or VGLUT2- respectively). Comparisons of general synapse characteristics, synapse density and size distribution were also done using these two variables. For the subset of pre-synaptic boutons containing mitochondria, synapses were additionally categorized based on mitochondria morphology (normal or damaged). The five ultrastructural features were: pre-synaptic bouton volume, pre-synaptic mitochondria volume, post-synaptic spine volume, PSD area, and number of post-synaptic spines associated with each pre-synaptic bouton. All raw area and volumetric quantifications of object contours were tabulated on a Microsoft Excel spreadsheet. The mean, standard deviation, and standard errors were calculated for each feature. Raw data tables were exported as .csv files and imported into MATLAB where all data analyses were performed. Comparisons were done on all quantitative features based on categorical variable groups using two-tailed Student's *T* tests. Differences of synapse size are shown on boxplots. Differences of synapse density are represented on scatter plots. Linear regression analyses were performed to assess relationships between pre- and post-synaptic ultrastructural

features for VGLUT2+ and VGLUT2- synapses. All features were expressed as Pearson product-moment coefficients for a first-degree polynomial. Initially, the ultrastructural measurements were not normally distributed. With the removal of outliers beyond three standard deviations from the mean and a log transformation of the data, quartile-quartile plots and Kolmogorov-Smirnov (K-S) tests confirmed that the data was normally distributed. Each ultrastructural feature was divided into 15 equally spaced bins. Binned data was used to generate normalized relative and cumulative frequency functions to examine differences in synapse size distribution based on genotype. Standard error values were calculated per bin and shown on the error bars. Two-tailed student *T* tests were done to compare size values between genotypes based on bin. To assess whether the levels of each categorical variable significantly influence changes observed among ultrastructural features, combinations of two categorical variables (each with two levels) and one dependent ultrastructural feature were inputted in nine separate 2x2 factorial analysis of variances (ANOVA) tests. All ANOVAs followed an unbalanced design without replication and computed constrained Type III sum of squares using the anovan function in MATLAB. Bonferroni *post hoc* tests were performed to assess significant interactions and effects.

For confocal microscopy studies, all .csv files from ImageJ particle and colocalization analyses were imported into MATLAB. Data was divided into three groups based on the region of the striatum along the rostral to caudal direction: rostral, middle, and caudal. For each section, the average optical densities of mHTT (channel 2: 546) and VGLUT2 (channel 3: 647) was computed for each ROI across the entire 20 $\mu$m image

stack. For each section, the average fractional percent area of each ROI mean was computed to determine the mean particle density values for each channel. The same steps were performed for computing the density of dual labelled VGLUT2 / mHTT particles. To assess distribution of synaptic density based on anatomical location within the striatum, between and within-species comparisons of VGLUT2 distribution were performed for each region of the striatum. Similar within-species comparisons were made for mHTT and dual labelled VGLUT2/mHTT density distribution among $Q175^{+/-}$ sections to determine whether significant regional differences are seen in the striatum. All figures were generated in MATLAB. The threshold of significance was set to $\alpha = 0.05$ for all statistical and *post hoc* tests.

## RESULTS

### *3D EM Reconstructions of VGLUT2+ & VGLUT2- Synapses*

Serial electron microscopy was used to characterize the distribution and ultrastructural properties of VGLUT2+ and VGLUT2- boutons forming excitatory asymmetric synapses (VGLUT2+ and VGLUT2- synapses) in the striatal neuropil of wildtype and $Q175^{+/-}$ animals. A total of 288 boutons with axospinous synapses (106 wildtype, 182 $Q175^{+/-}$) from 5 subjects (2 wildtype, 3 $Q175^{+/-}$) were reconstructed in 3D using Reconstruct™ software. DAB was used to immunolabel VGLUT2 (see methods). Differences between VGLUT2+ and VGLUT2- synapses as they appear on EM micrographs can be seen in Figure 6. In total, 138 VGLUT2+ (56 wildtype, 82 $Q175^{+/-}$) and 150 VGLUT2- (50 wildtype, 100 $Q175^{+/-}$) synapses were reconstructed. All synapses were characterized from 23 randomly placed counting fields. A total area of 1,472 $\mu m^2$ was analyzed, equating to a total volume of 1,030.4 $\mu m^3$. While the relative number of characterized VGLUT2+ and VGLUT2- synapses were similar, all wildtype synapses came from 5 of 23 counting frames (sectional area = 320 $\mu m^2$; volume = 224 $\mu m^3$).

For this study, only axospinous excitatory synapses were characterized. All axodendritic synapse characteristics collected during data acquisition stage were omitted from statistical analyses. Criteria for consideration for excitatory synapses include the presence of these synaptic elements: a wide synaptic cleft, asymmetric pre- and post-

synaptic elements, round synaptic vesicles, and a dense post-synaptic density (PSD) (Peters et al., 1991). Identified excitatory synapses were evaluated for completeness as follows – it must be composed of complete pre-synaptic bouton, post-synaptic spine, and PSD. Complete synapses typically span ~10-30 serial sections in our datasets. For each synapse, shape contours were generated for pre-synaptic boutons and post-synaptic spines. Line contours of the synapse at the junction between the pre-synaptic bouton and PSD were also created. Specific morphological features were identified to further characterize the synapses. All completed synapses were defined based on their genotype (wildtype or $Q175^{+/-}$), whether the synapses have a non-perforated (continuous) or a perforated (interrupted) PSD, whether the pre-synaptic bouton was multi-synaptic (MSB), the number of mitochondria found within the pre-synaptic bouton, and if the mitochondria were normal or damaged. Mitochondria were considered damaged if there was evidence of morphological alterations such as mitochondrial fission, fragmentation, and disorganized dilated cristae (Costa et al., 2010). All object contours and characterizations were made for the entire volume of each synapse and can be seen on EM micrographs. Reconstruct™ software was used to generate a 3D model (Virtual Reality Modeling Language) of all synapses. Object contours of synaptic elements in different counting fields (Fig. 7A) and individual wildtype (Fig. 7B, C) and Q175 (Fig. 7D, E) axospinous synapses were rendered and observed in 3D.

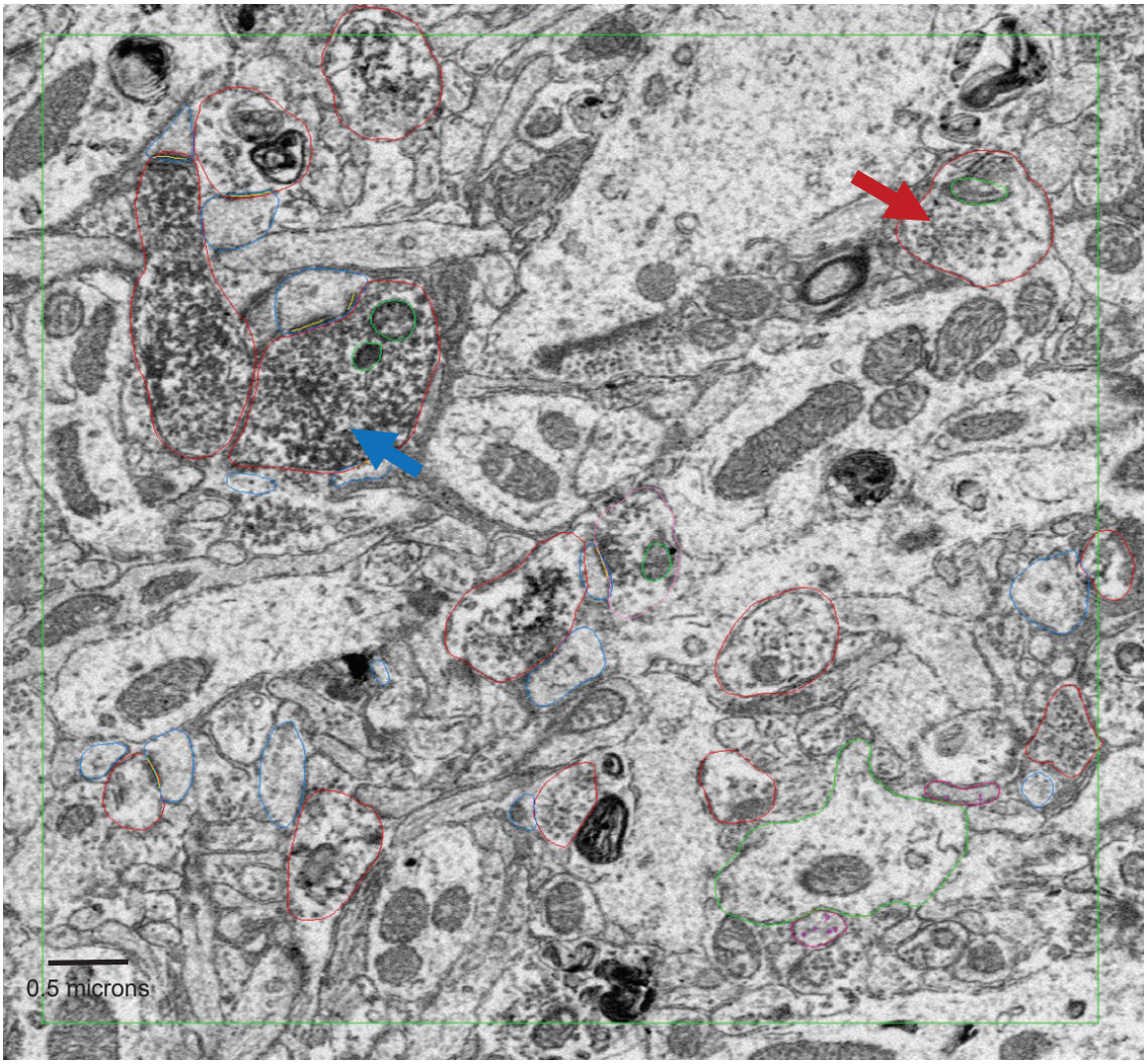


**Figure 6: EM micrograph of VGLUT2+ & VGLUT2- axon terminals.** Counting frame of an EM micrograph showing the difference between a VGLUT2+ synapse (blue arrow) and a VGLUT2- synapse (red arrow). The characteristic dark precipitate of DAB can be seen within the round vesicles of the soma in the VGLUT2+ synapse. Scale: 0.5 microns

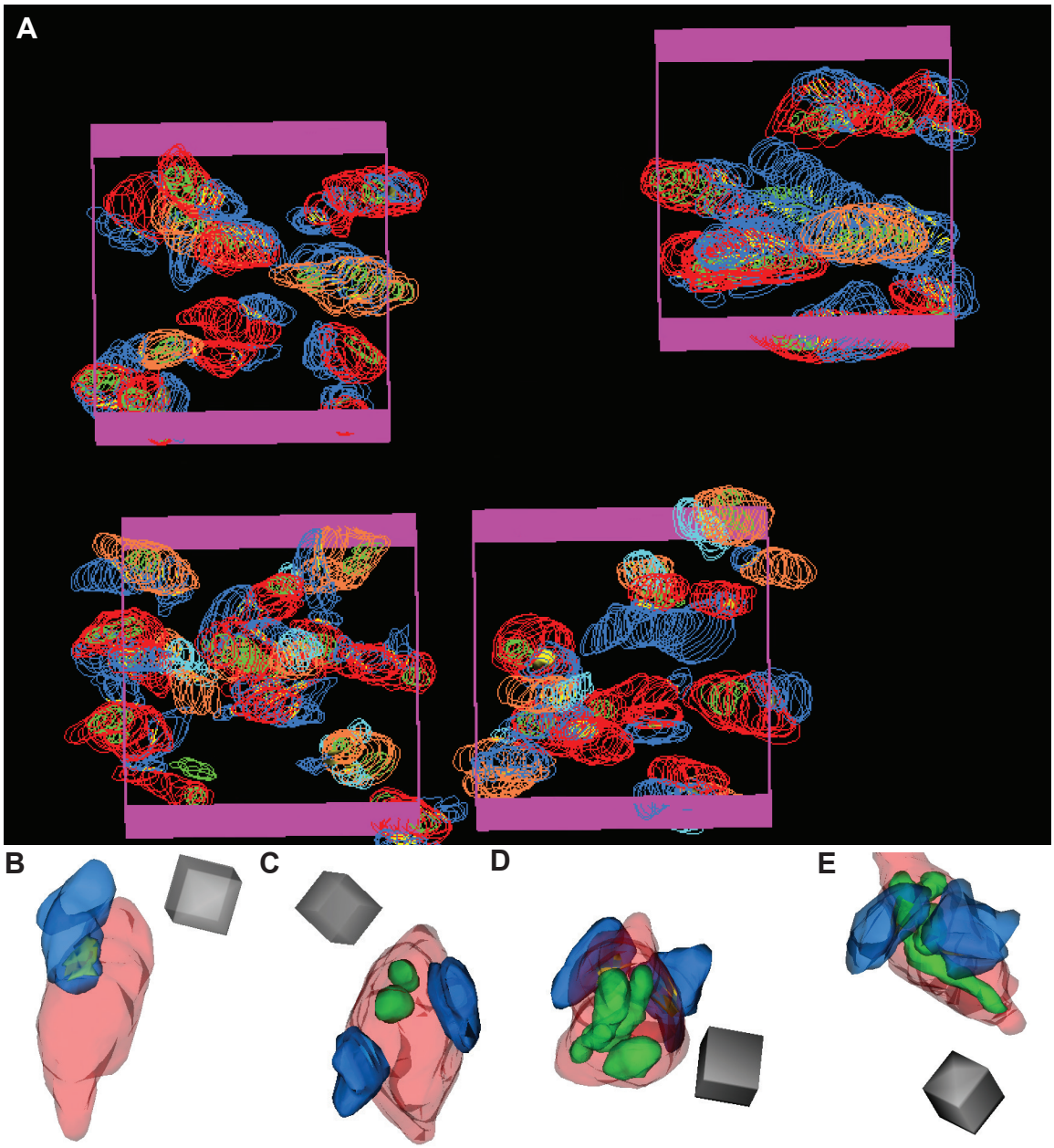


**Figure 7: 3D model of reconstructed axospinous synapses.** Object contours (red & orange: pre-synaptic boutons; blue & cyan: dendritic spines; green: mitochondria; yellow: area of synapse between the PSD and pre-synaptic bouton) of reconstructed VGLUT2+ and VGLUT2- synapses from 4 randomly placed counting fields (magenta) in a wildtype mouse (A). 3D reconstructed wildtype axospinous synapse associated with one dendritic spine (B), two dendritic spines and two mitochondria (C). 3D reconstructed Q175 axospinous synapse associated with two dendritic spines and fragmented mitochondria (D), two dendritic spines and elongated mitochondria (E). Red: pre-synaptic boutons; Blue: dendritic spines; green: mitochondria; yellow: area of synapse between the PSD and pre-synaptic bouton. Scale cube: 0.7 x 0.7 x 0.7 microns

***Characterization of VGLUT2+ & VGLUT2- Synapses***

For each element in a counted synapse, volumetric measurements of pre-synaptic boutons, pre-synaptic mitochondria, and post-synaptic spines were exported in addition to area measurements of the synaptic junction of the PSD. After object contours were created for all synaptic elements, ultrastructural variables were quantitatively compared between wildtype and $Q175^{+/-}$ animals were performed (Table 1). Characterization of synapses shows that the proportion of macular (n = 33) and perforated (n = 23) VGLUT2+ synapses did not differ in wildtype animals (Fig. 8A). Additionally, 20% of all wildtype boutons were multi-synaptic (now referred to as MSB) (n = 17), synapsing onto two or more post-synaptic spines (Fig. 8B). In $Q175^{+/-}$ animals there was a higher proportion of macular (n = 66) than perforated (n = 16) synapses (Fig. 8A). Relative proportions of multi-synaptic boutons in $Q175^{+/-}$ animals (n = 18) were comparable to the wildtype group, consisting of 22% of all reconstructed pre-synaptic boutons (Fig. 8B).

The ultrastructural properties of VGLUT2- axospinous synapses were also compared between wildtype and $Q175^{+/-}$ animals. The proportion of macular (n = 27) and perforated (n = 23) VGLUT2- synapses did not differ in wildtype animals (Fig. 8C), with MSBs (n = 10) making up 20% of all reconstructed boutons (Fig. 8D). In $Q175^{+/-}$ animals, there was a higher proportion of macular (n = 63) than perforated (n = 37) synapses (Fig. 8C). Relative proportions of multi-synaptic boutons in $Q175^{+/-}$ animals (n = 24) did not differ from the wildtype group (Fig. 8D).

**VGLUT2+ Axospinous Synapses**

| | Bouton Volume ($\mu m^3$) | Pre-synaptic Mitochondria Volume ($\mu m^2$) | Spine Volume ($\mu m^2$) | PSD Area ($\mu m^2$) |
|---|---|---|---|---|
| wildtype (n = 56) | 0.99 ± 0.07 | 0.13 ± 0.01 | 0.36 ± 0.03 | 0.30 ± 0.02 |
| $Q175^{+/-}$ (n = 82) | 0.88 ± 0.04 | 0.10 ± 0.006 * | 0.19 ± 0.01 *** | 0.24 ± 0.01 * |

**VGLUT2- Axospinous Synapses**

| | Bouton Volume ($\mu m^3$) | Pre-synaptic Mitochondria Volume ($\mu m^2$) | Spine Volume ($\mu m^2$) | PSD Area ($\mu m^2$) |
|---|---|---|---|---|
| wildtype (n = 50) | 0.73 ± 0.07 | 0.10 ± 0.01 | 0.26 ± 0.04 | 0.24 ± 0.02 |
| $Q175^{+/-}$ (n = 100) | 0.85 ± 0.04 | 0.08 ± 0.004 | 0.28 ± 0.02 | 0.28 ± 0.02 |

**Table 1: Means (± SEM) of VGLUT2+ & VGLUT2- ultrastructural features.** Averages for VGLUT2+ (top) and VGLUT2- (bottom) axospinous synapses given with SEM. No significant differences found in VGLUT2- wildtype and $Q175^{+/-}$ groups. Spine volume: $p = 1.02 \times 10^{-6}$; Mitochondria volume: $p = 0.035$; PSD Area: $p = 0.019$. * $p < 0.05$; ** $p < 0.005$; *** $p < 0.0005$

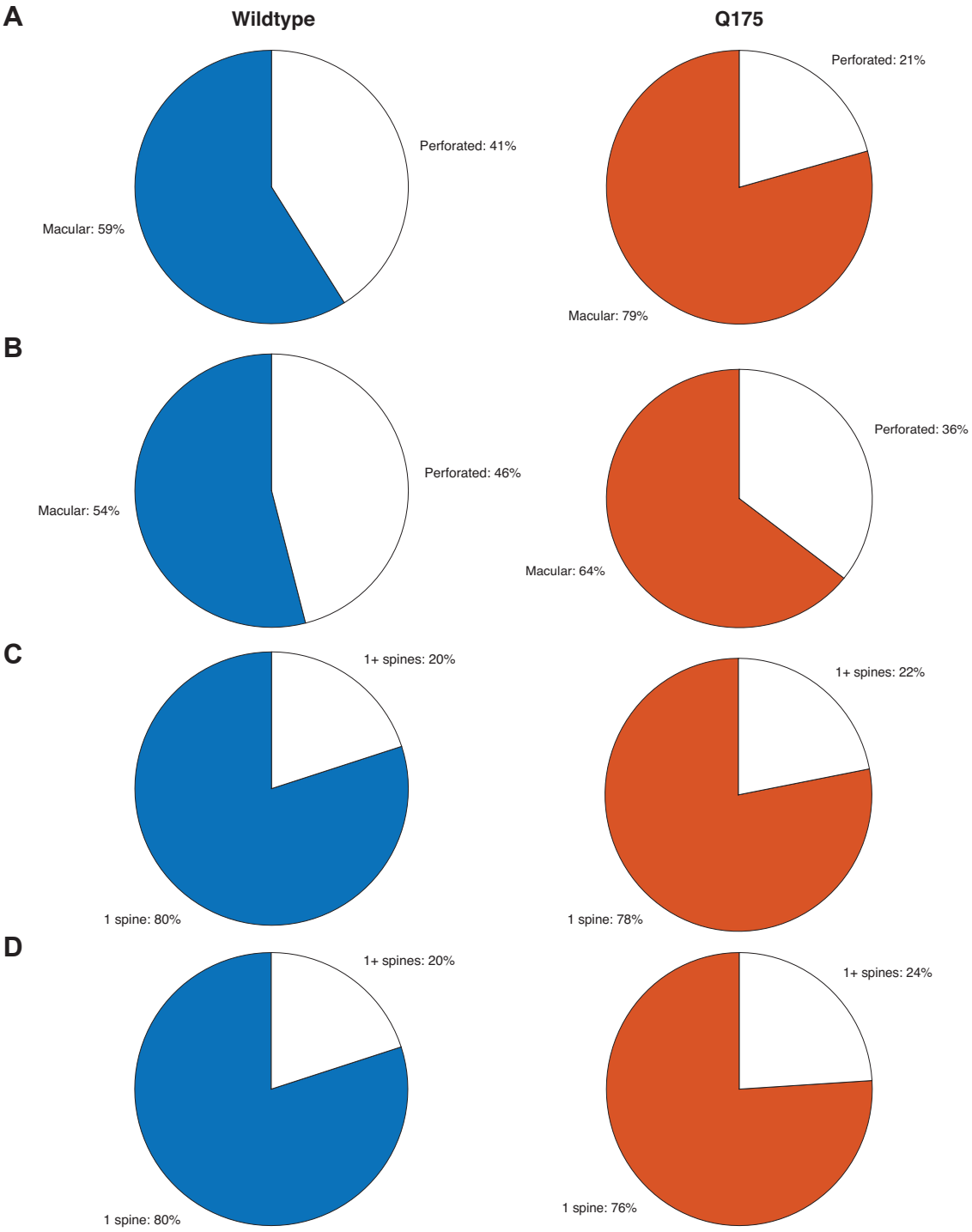


**Figure 8: Morphology and targets of VGLUT2+ and VGLUT2- boutons.** Relative proportions of VGLUT2+ boutons (A, B) forming macular and perforated synapses (A) and multi-synaptic and single synapses on spines (B) in wildtype (left, blue) and Q175 (right, red) groups. Relative proportions of VGLUT2- boutons (C, D) forming macular and perforated synapses (C) and multi-synaptic and single synapses on spines (D) in wildtype (left) and Q175 (right) groups.

For VGLUT2+ pre-synaptic boutons containing mitochondria, 32% (n = 11) of synapses had the appearance of being damaged in wildtype and 65% (n = 48) had this appearance in $Q175^{+/-}$ synapses (Fig. 9A). In VGLUT2- pre-synaptic boutons containing mitochondria, 21% (n = 4) and 71% (n = 55) of the mitochondria appeared damaged in wildtype and $Q175^{+/-}$ animals respectively (Fig. 9B). Quantitative comparisons of mitochondria volume revealed only a significant difference in VGLUT2+ boutons – $Q175^{+/-}$ mitochondria pre-synaptic mitochondria were significantly smaller compared to wildtype (mitochondria volume: $p = 0.04$, Fig. 9C). Characteristics of normal versus damaged mitochondria can be seen on electron micrograph sections (Fig. 9D, E) as well as in the 3D reconstructed mitochondria (Fig. 9F, G). Damaged mitochondria in both $Q175^{+/-}$ VGLUT2+ and VGLUT2- pre-synaptic boutons consistently demonstrate fragmentation from a single whole element to smaller "pea-shaped" fragments (Fig. 9D, F). Elongation of mitochondria was also observed (Fig. 9E, G). Results support observations of reduced volume and aberrant mitochondria morphology observed in the striatum of the YAC128 HD mouse model (Song et al., 2011).

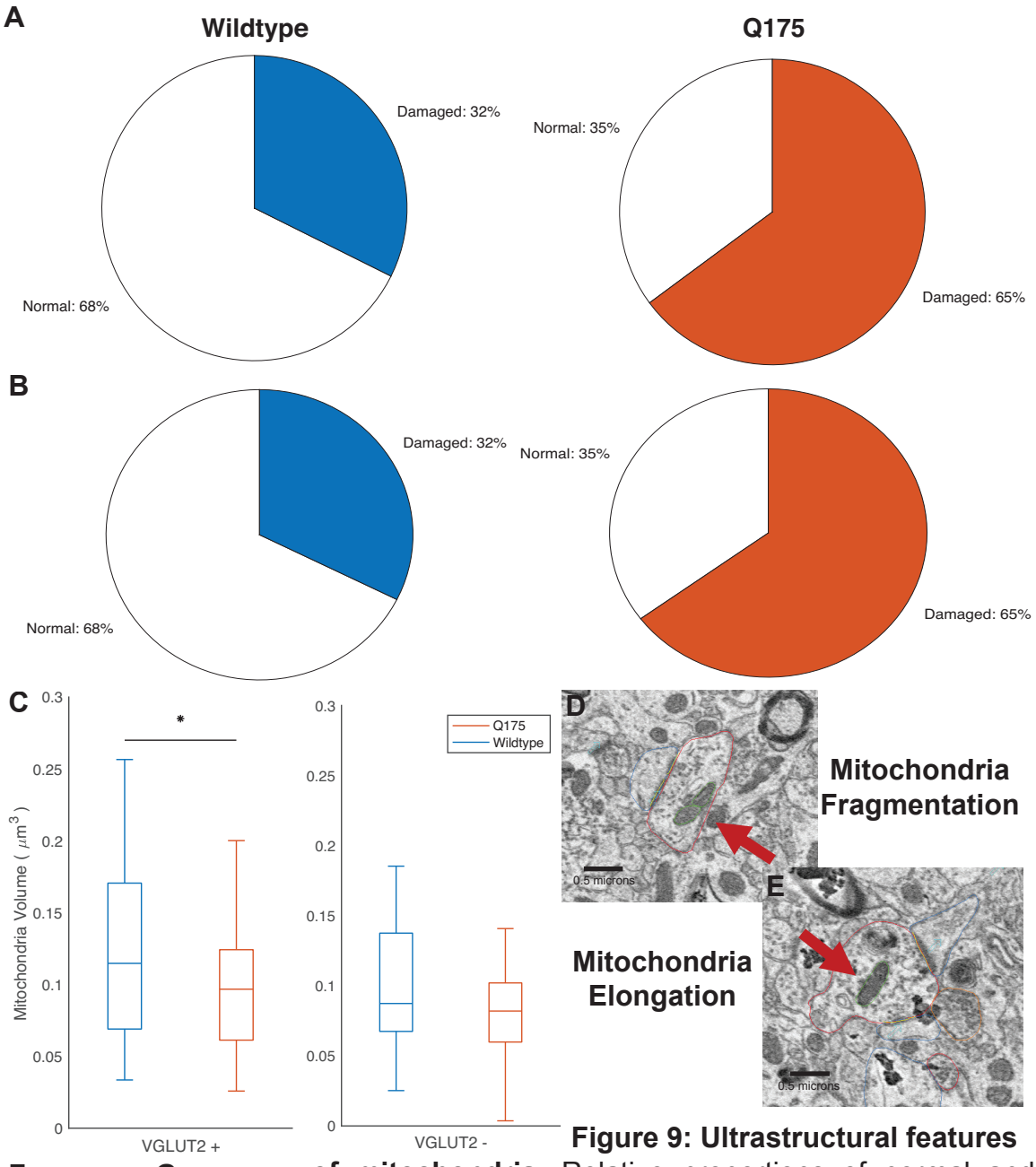


**Figure 9: Ultrastructural features of mitochondria.** Relative proportions of normal and damaged mitochondria in VGLUT2+ (A) and VGLUT2- (B) boutons of wildtype (left, blue), and Q175 (right, red) dorsal striatum.Comparisons of average mitochondria volume between wildtype and Q175 mice in VGLUT2+ (left) and VGLUT2- (right) boutons (C). Electron micrographs showing signs of mitochondrial fission (red arrows) in VGLUT2+ synapses, including fragmentation into smaller elements (D) and abnromal elongation (E) 3D reconstructions for mitochondria in (D) and (E) (F, G). * $p < 0.05$.

### *Comparison of VGLUT2+ & VGLUT2- Synapse Size*

To assess differences in synapse size between VGLUT2+ and VGLUT2- synapses, comparisons of pre-synaptic bouton volume, post-synaptic spine volume, and PSD area across were made between wildtype and $Q175^{+/-}$ groups. VGLUT2+ post-synaptic spine volume and PSD area revealed significant differences (all $p < 0.05$, Student's *T* test) between wildtype and $Q175^{+/-}$ groups (spine volume: $p = 1.02 \times 10^{-6}$, Fig. 10B; PSD area: $p = 0.019$, Fig. 10C). No differences between genotypes were observed for pre-synaptic bouton volume in VGLUT2+ synapses (Fig. 10A). Additionally, no differences between genotypes were for any ultrastructural features of VGLUT2- synapses. These results support previous findings demonstrating no change in pre-synaptic terminal size, but significant reductions in post-synaptic spine size at VGLUT2+ immunolabeled terminals in the R6/2 HD model (Parievsky et al., 2017).

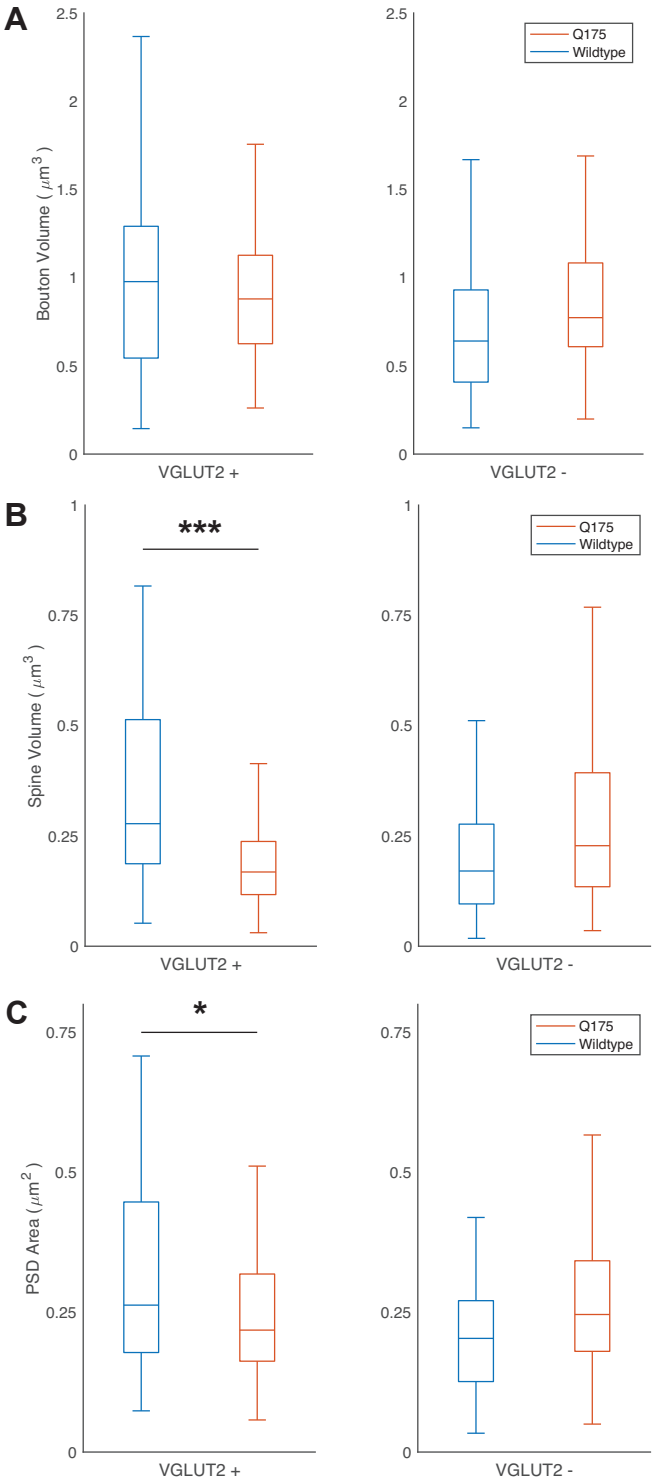


**Figure 10: Comparison of VGLUT2+ & VGLUT2- synapse size.** Box and whisker plots showing wildtype (blue) and Q175 (red) comparisons for VGLUT2+ (left) and VGLUT2- (right) bouton volume (A), and their associated spine volumes (B), and PSD areas (C). * $p < 0.05$; ** $p < 0.005$; *** $p < 0.0005$

***Distribution of VGLUT2+ & VGLUT2- Synapse Size***

To examine the distribution of VGLUT2+ and VGLUT2- synapse sizes, all features were divided into 15 bins. The relative frequency (number of measurements per bin / total number of measurements) was calculated per bin between wildtype and $Q175^{+/-}$ mice for VGLUT2+ (Fig. 11) and VGLUT2- synapses (Fig. 12). For bouton volume, there were significant differences in bin 3 (wildtype: $0.49 \pm 0.01\ \mu m^3$, $Q175^{+/-}$: $0.55 \pm 0.01\ \mu m^3$; $p = 0.01$; Fig. 11A) and bin 5 (wildtype: $0.81 \pm 0.02\ \mu m^3$, $Q175^{+/-}$: $0.67 \pm 0.008\ \mu m^3$; $p = 0.03$; Fig. 11A). For mitochondria volume, there was a significant difference in bin 9 (wildtype: $0.17 \pm 0.0007\ \mu m^3$, $Q175^{+/-}$: $0.16 \pm 0.001\ \mu m^3$; $p = 0.005$; Fig. 11C). For spine volume, there were significant differences in bin 5 (wildtype: $0.27 \pm 0.004\ \mu m^3$, $Q175^{+/-}$: $0.29 \pm 0.005\ \mu m^3$; $p = 0.01$; Fig. 11B) and bin 6 (wildtype: $0.36 \pm 0.001\ \mu m^3$, $Q175^{+/-}$: $0.34 \pm 0.005\ \mu m^3$; $p = 0.01$; Fig. 11C).

For PSD area, there was a significant difference in bin 3 (wildtype: $0.19 \pm 0.004\ \mu m^2$, $Q175^{+/-}$: $0.17 \pm 0.003\ \mu m^2$; $p = 0.04$; Fig. 11D). There was a leftward shift (higher frequency of smaller spines) for the cumulative distribution of VGLUT2+ $Q175^{+/-}$ spine volumes relative to wildtype (Kolmogorov-Smirnov test, $p = 0.03$; Fig. 11B). No other leftward shifts were seen. Among VGLUT2- synapses, the frequency distributions were not different between wildtype and $Q175^{+/-}$ features except for spine volume (Fig. 12C)

where differences were observed in bin 1 (wildtype: 0.05 ± 0.006 $\mu m^3$, $Q175^{+/-}$: 0.08 ± 0.005 $\mu m^3$; p = 0.01), bin 4 (wildtype: 0.29 ± 0.008 $\mu m^3$, $Q175^{+/-}$: 0.32), and bin 8 (wildtype: 0.63 ± 0.002 $\mu m^3$, $Q175^{+/-}$: 0.64 ± 0.01 $\mu m^3$; p = 0.03).

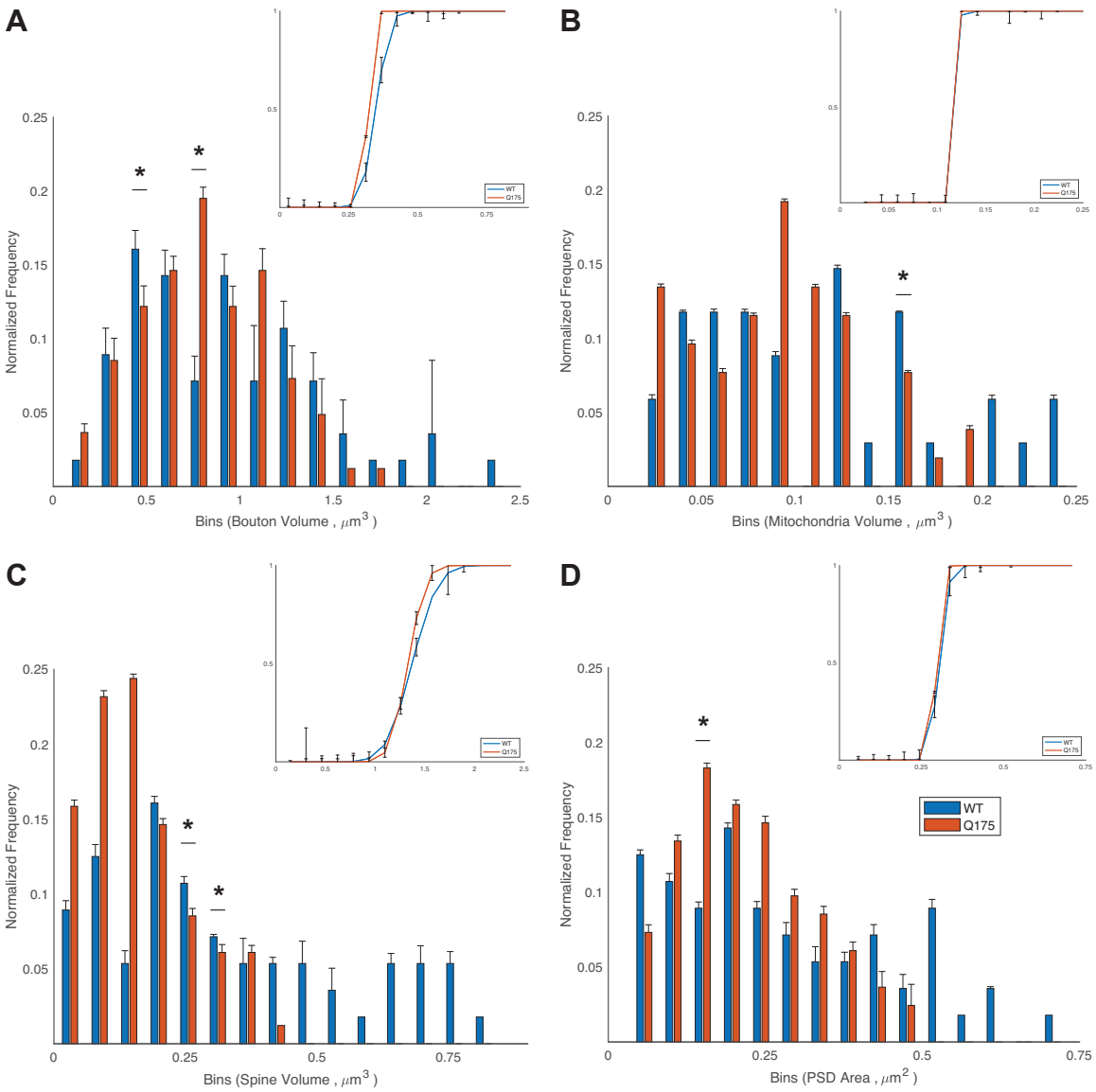


**Figure 11: Distribution of VGLUT2+ ultrastructural features.** Relative frequency (main) and cumulative distribution (upper right) based on binned measurements of bouton volume (A), mitochondria volume (B), spine volume (C), and PSD area (D). * $p < 0.05$

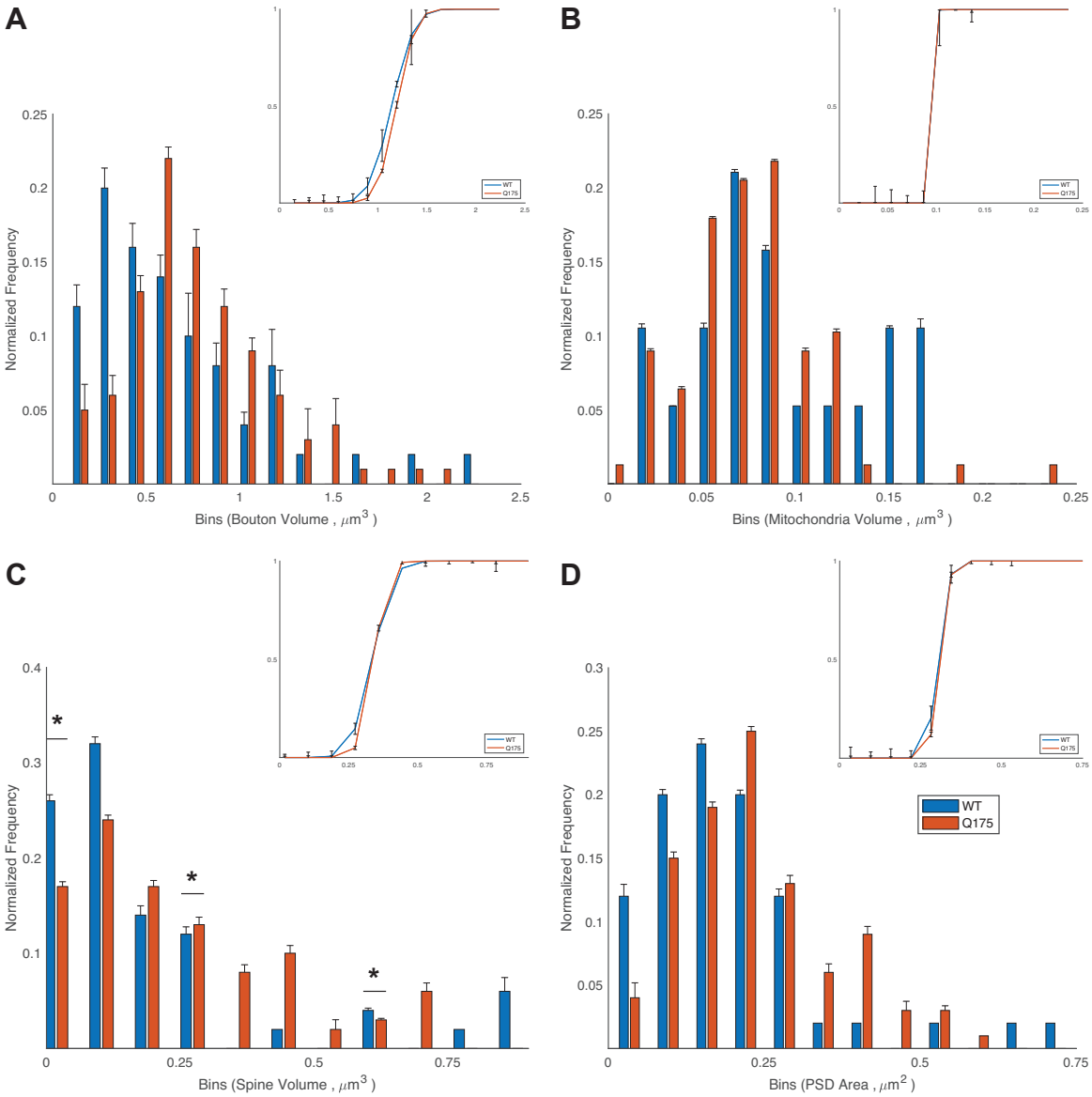


**Figure 12: Distribution of VGLUT2- ultrastructural features.** Relative frequency (main) and cumulative distribution (upper right) based on binned measurements of bouton volume (A), mitochondria volume (B), spine volume (C), and PSD area (D). * $p < 0.05$

***Density of VGLUT2+ & VGLUT2- Synapses***

To estimate differences in the spatial abundance between VGLUT2+ & VGLUT2- synapses in wildtype and $Q175^{+/-}$ mice, a size frequency method from 1975 was employed to calculate the numerical density of all synapses (Colonnier & Beaulieu, 1985). This method has been previously used in our lab for quantification of synapse density in EM micrographs (Peters, Sethares, & Luebke, 2008). To calculate synapse density, the empirical formula $N_V = N_A / D$ is used. $N_V$ represents the number of synapses per unit volume, $N_A$ represents the number of synaptic junctions per unit area of a random counting field on an EM micrograph, and D represents the average length of PSD line contours that are associated with the synaptic junction. Comparisons of synaptic densities between wildtype and $Q175^{+/-}$ mice (all $p < 0.05$, Student's *T* test) reveal ~2x reductions in synapse density in $Q175^{+/-}$ mice for both VGLUT2+ ($p < 0.05$; Fig. 13) and VGLUT2- ($p < 0.05$; Fig. 13) synapses. The same ~2x reduction was also observed in a between all wildtype and $Q175^{+/-}$ synapses ($p < 0.05$). All density values are reported in Table 2.

| | VGLUT2+ (synapses / $mm^3$) | VGLUT2- (synapses / $mm^3$) | Total |
|---|---|---|---|
| wildtype | $0.20 \pm 0.02$ | $0.23 \pm 0.02$ | $0.42 \pm 0.02$ |
| $Q175^{+/-}$ | $0.10 \pm 0.01$ * | $0.11 \pm 0.02$ * | $0.22 \pm 0.01$ * |

**Table 2: Means (± SEM) of VGLUT2+ & VGLUT2- synapse density in the dorsal striatum**. Average VGLUT2+ (left), VGLUT2- (middle) and total (right) synapse density found in wildtype (first row) and $Q175^{+/-}$ groups (second row) * $p < 0.05$

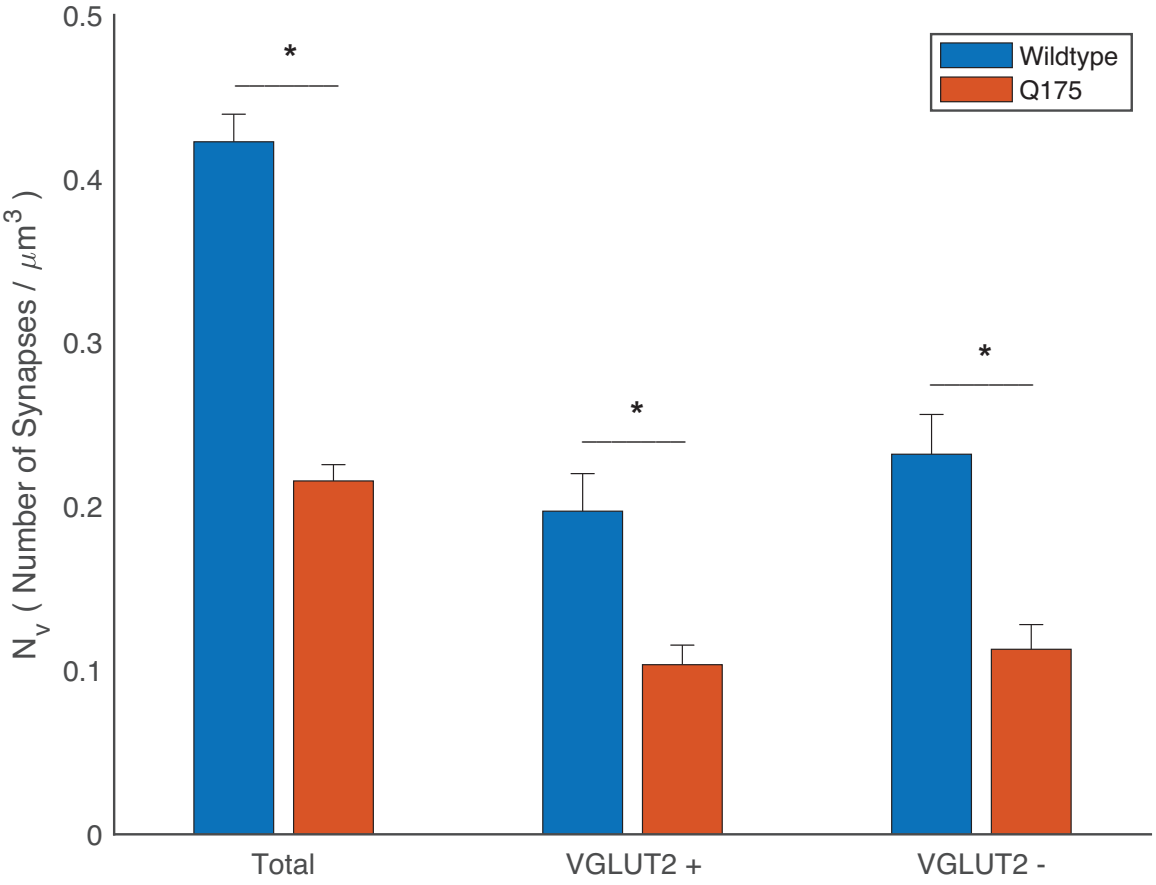


**Figure 13: Density of VGLUT2+ & VGLUT2- synapses.** Numerical density per unit volume of all (VGLUT2+ & VGLUT2-) synapses (left), VGLUT2+ synapses (middle), and VGLUT2- synapses (right), in wildtype (blue) and Q175 (red) groups. * $p < 0.05$

***Relationships Between Pre- & Post-Synaptic Elements***

To assess whether the properties of 3D reconstructed pre-synaptic elements were related to their respective post-synaptic elements, linear regression analyses for pre-synaptic bouton volume x post-synaptic spine volume; pre-synaptic bouton volume x PSD area; and post-synaptic spine volume x PSD area were performed for both VGLUT2+ and VGLUT2- ultrastructural features in wildtype and $Q175^{+/-}$ mice (Figure 14). After performing linear regression analyses between bouton volume and spine volume, positive correlations were seen for both VGLUT2+ (wildtype, $r = 0.56$; $Q175^{+/-}$, $r = 0.32$; $p < 0.01$; Fig. 14A, left) and VGLUT2- synapses (wildtype, $r = 0.69$; $Q175^{+/-}$, $r = 0.39$; $p < 0.01$; Fig. 14A, right). Regression analyses examining the relationship between bouton volume and PSD area also demonstrated positive correlations for VGLUT2+ synapses (wildtype, $r = 0.54$; $Q175^{+/-}$, $r = 0.46$; $p < 0.01$; Fig. 14B, left), with stronger positive correlations among VGLUT2- synapses (wildtype, $r = 0.63$; $Q175^{+/-}$, $r = 0.60$; $p < 0.01$; Fig. 14B, right). The strongest positive correlations were seen between PSD area and spine volume in VGLUT2+ (wildtype, $r = 0.82$; $Q175^{+/-}$, $r = 0.72$; $p < 0.01$; Fig. 14C, left) and VGLUT2- synapses (wildtype, $r = 0.90$; $Q175^{+/-}$, $r = 0.77$; $p < 0.01$; Fig. 14C, right).

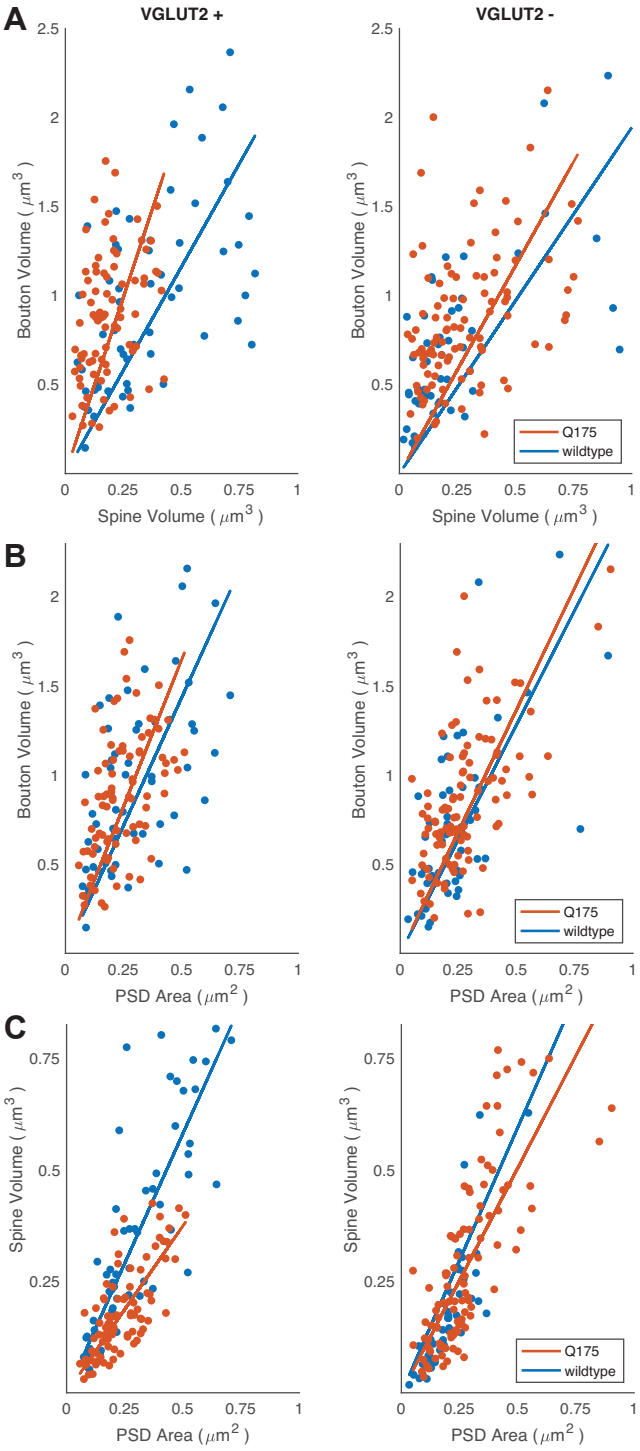


**Figure 14: Linear regressions of VGLUT2+ & VGLUT2- ultrastructural features.** Scatterplots demonstrating relationships between pre- and post-synaptic features for VGLUT2+ (left) and VGLUT2- (right) synapses ultrastructural features: bouton volume x spine volume (A), bouton volume x PSD area (B), spine volume x PSD area (C) for wildtype (blue) and Q175 (red) groups.

***Relationship Between Group Characteristics & Ultrastructural Features***

To assess the relationships between synapse categorical variables and ultrastructural features, a total of ten two-way unbalanced ANOVAs without replication were performed. The first seven ANOVAs were performed with two categorical factors, each with two levels: genotype (wildtype, $Q175^{+/-}$), and VGLUT2 marker (VGLUT2+, VGLUT2-). The first three ANOVAs examined the relationship between the two categorical factors and the following ultrastructural features for all synapses (n = 288): bouton volume, spine volume and PSD area. The next four ANOVAs examined the same relationships, but with the addition of an ANOVA for mitochondria volume in synapses containing mitochondria (n = 182). Output tables for these ANOVAs are found in Table 3.

For the ANOVAs of bouton volumes among all synapses, the main effect genotype was not significant ($F [1, 284] = 2.16, p > 0.05$) while the main effect of VGLUT2 marker was significant ($F [1, 284] = 10.28, p = 0.0015$; Table 3A), suggesting that the average bouton volume was significantly larger in all VGLUT2+ synapses ($0.93 \pm 0.04\ \mu m^3$) than in all VGLUT2- ($0.81 \pm 0.03\ \mu m^3$) synapses. The interaction between genotype and VGLUT2 marker was significant ($F [1, 284] = 5.7, p = 0.0176$; Table 3A), suggesting that the effect of VGLUT2 marker was greater in wildtype boutons than in $Q175^{+/-}$ boutons ($p = 0.003$). In analyses for mitochondria-containing synapses, the main effect of genotype was significant ($F [1, 179] = 6.56, p = 0.0113$; Table 3D) while the main VGLUT2 marker was not significant ($F [1, 179] = 3.5, p > 0.05$; Table 3D), suggesting that the average bouton volume was significantly larger in wildtype synapses ($1.18 \pm 0.07\ \mu m^3$) than in

$Q175^{+/-}$ synapses (0.95 ± 0.03 $\mu m^3$). No significant interaction was observed between genotype and VGLUT2 marker ($F [1, 179] = 0.79$, $p > 0.05$; Table 3D).

ANOVAs of spine volume did not yield significant main effects for genotype ($F [1, 284] = 2.45$, $p > 0.05$) or VGLUT2 marker ($F [1, 284] = 1.15$, $p > 0.05$), but a significant interaction ($F [1, 284] = 23.55$, $p = 2.01 \times 10^6$; Table 3B) suggests that the effect of genotype was greater in VGLUT2+ than VGLUT2- spines ($p = 0.0001$) for all synapses. The same analyses for synapses with mitochondria yielded a significant main effect for genotype ($F [1, 179] = 13.1$, $p = 0.0004$; Fig. 15F), but not for VGLUT2 marker ($F [1, 179] = 0.8154$, $p > 0.05$; Table 3F), suggesting that the average spine volume was significantly larger in wildtype synapses (0.43 ± 0.04 $\mu m^3$) than in $Q175^{+/-}$ synapses (0.25 ± 0.01 $\mu m^3$). ANOVAs for PSD areas among all synapses reveal no significant main effects for genotype ($F [1, 284] = 0.06$, $p > 0.05$; Table 3C) or VGLUT2 marker, ($F [1, 284] = 1.1$, $p > 0.05$; Table 3C). However, a significant interaction ($F [1, 284] = 6.7$, $p = 0.0101$; Fig. 15C) between the two categorical variables was initially reported but determined to be non-significant after post hoc analyses (Bonferroni *post hoc* test, $p > 0.05$). When the same analyses were performed for PSD areas for synapses containing mitochondria, the same results were observed for genotype ($F [1, 179] = 3.49$, $p > 0.05$; Table 3G) and VGLUT2 marker ($F [1, 179] = 0.29$, $p > 0.05$; Table 3G), and no significant interaction was reported ($F [1, 179] = 3.59$, $p > 0.0$; Table 3G). ANOVAs of mitochondria volume yielded a significant main effect of genotype ($F [1, 179] = 4.28$, $p = 0.04$; Table 3E), suggesting that the average mitochondria volume was significantly larger in wildtype boutons (0.12 ±

0.009 $\mu m^3$) than in $Q175^{+/-}$ boutons (0.09 ± 0.004 $\mu m^3$). The main effect for VGLUT2 marker ($F [1, 179] = 3.82$, $p > 0.05$; Fig. 15E) and interaction ($F [1, 179] = 0.1$, $p > 0.05$; Table 3E), was not significant.

In the remaining three ANOVAs, genotype (wildtype, $Q175^{+/-}$) and mitochondria morphology (normal, damaged), were the categorical factors used for analyses of the same ultrastructural features used in the first three ANOVAs (Table 4). The features in these analyses were also from the subset of synapses containing mitochondria. Genotype was a significant main effect in all three analyses: bouton volume: $F (1, 179) = 14.95$, $p = 0.0002$; Table 4A; spine volume: $F (1, 179) = 16.56$, $p = 0.0001$; Table 4B; PSD area: $F (1, 179) = 4.86$, $p = 0.0287$; Table 4C. All main effects suggest a pattern where the average ultrastructural feature was significantly larger in wildtype synapses with normal mitochondria (bouton volume: 1.18 ± 0.07 $\mu m^3$; spine volume: 0.43 ± 0.04 $\mu m^3$; PSD area: 0.34 ± 0.03 $\mu m^2$) when compared to $Q175^{+/-}$ synapses with normal mitochondria (bouton volume: 0.95 ± 0.03 $\mu m^3$; spine volume: 0.25 ± 0.01 $\mu m^3$; PSD area: 0.28 ± 0.01 $\mu m^2$). Mitochondria morphology was only a significant main effect in the ANOVA for bouton volume ($F [1, 179] = 5.47$, $p = 0.0205$; Table 4A), suggesting the same pattern of larger wildtype boutons and smaller $Q175^{+/-}$ boutons as observed for the genotype main effect. In all three ANOVAs, no significant interactions were reported. ANOVAs results for genotype x VGLUT2 marker and genotype x mitochondria morphology are summarized in Figures 15 and 16 respectively.

**A** Genotype x VGLUT2 Marker - Bouton Volume

| Source | Sum Sq. | d.f. | Mean Sq. | F | Prob>F |
|---|---|---|---|---|---|
| Genotype | 0.5726 | 1 | 0.5726 | 2.16 | 0.143 |
| Vglut2 Marker | 2.73 | 1 | 2.72996 | 10.28 | 0.0015 |
| Genotype * Vglut2 Marker | 1.5132 | 1 | 1.51321 | 5.7 | 0.0176 |
| Error | 75.3935 | 284 | 0.26547 | | |
| Total | 79.2392 | 287 | | | |

**B** Genotype x VGLUT2 Marker - Spine Volume

| Source | Sum Sq. | d.f. | Mean Sq. | F | Prob>F |
|---|---|---|---|---|---|
| Genotype | 1.33 | 1 | 1.33 | 2.45 | 0.1183 |
| Vglut2 Marker | 0.626 | 1 | 0.6257 | 1.15 | 0.2835 |
| Genotype * Vglut2 Marker | 12.761 | 1 | 12.7608 | 23.55 | 0 |
| Error | 153.901 | 284 | 0.5419 | | |
| Total | 167.988 | 287 | | | |

**C** Genotype x VGLUT2 Marker - PSD Area

| Source | Sum Sq. | d.f. | Mean Sq. | F | Prob>F |
|---|---|---|---|---|---|
| Genotype | 0.0199 | 1 | 0.0199 | 0.06 | 0.8015 |
| Vglut2 Marker | 0.3449 | 1 | 0.34493 | 1.1 | 0.2958 |
| Genotype * Vglut2 Marker | 2.1066 | 1 | 2.10661 | 6.7 | 0.0101 |
| Error | 89.3049 | 284 | 0.31445 | | |
| Total | 91.4743 | 287 | | | |

**D** Genotype x VGLUT2 Marker - Bouton Volume

| Source | Sum Sq. | d.f. | Mean Sq. | F | Prob>F |
|---|---|---|---|---|---|
| Genotype | 1.0211 | 1 | 1.02105 | 6.56 | 0.0113 |
| Vglut2 Marker | 0.5448 | 1 | 0.54481 | 3.5 | 0.063 |
| Genotype * Vglut2 Marker | 0.1228 | 1 | 0.12276 | 0.79 | 0.3757 |
| Error | 27.8614 | 179 | 0.15565 | | |
| Total | 29.962 | 182 | | | |

**E** Genotype x VGLUT2 Marker - Mitochondria Volume

| Source | Sum Sq. | d.f. | Mean Sq. | F | Prob>F |
|---|---|---|---|---|---|
| Genotype | 1.335 | 1 | 1.33501 | 4.28 | 0.04 |
| Vglut2 Marker | 1.1904 | 1 | 1.19036 | 3.82 | 0.0523 |
| Genotype * Vglut2 Marker | 0.0313 | 1 | 0.0313 | 0.1 | 0.7518 |
| Error | 55.8493 | 179 | 0.31201 | | |
| Total | 59.3365 | 182 | | | |

**F** Genotype x VGLUT2 Marker - Spine Volume

| Source | Sum Sq. | d.f. | Mean Sq. | F | Prob>F |
|---|---|---|---|---|---|
| Genotype | 6.41 | 1 | 6.41045 | 13.1 | 0.0004 |
| Vglut2 Marker | 0.027 | 1 | 0.02676 | 0.05 | 0.8154 |
| Genotype * Vglut2 Marker | 5.05 | 1 | 5.05024 | 10.32 | 0.0016 |
| Error | 87.587 | 179 | 0.48931 | | |
| Total | 101.097 | 182 | | | |

**G** Genotype x VGLUT2 Marker - PSD Area

| Source | Sum Sq. | d.f. | Mean Sq. | F | Prob>F |
|---|---|---|---|---|---|
| Genotype | 0.9816 | 1 | 0.98156 | 3.49 | 0.0633 |
| Vglut2 Marker | 0.0822 | 1 | 0.08221 | 0.29 | 0.5893 |
| Genotype * Vglut2 Marker | 1.0079 | 1 | 1.00789 | 3.59 | 0.0599 |
| Error | 50.3233 | 179 | 0.28114 | | |
| Total | 52.6636 | 182 | | | |

**Table 3: 2x2 Factorial ANOVA output tables for Genotype x VGLUT2 Marker.** ANOVA results examining ultrastructural features for all synapses: bouton volume (A), spine volume (B), PSD area (C). ANOVA results examining ultrastructural features for synapses containing mitochondria: bouton volume (D), mitochondria volume (E), spine volume (F), PSD area (G).

**A** Genotype x Mitochondria Morphology - Bouton Volume

| Source | Sum Sq. | d.f. | Mean Sq. | F | Prob>F |
|---|---|---|---|---|---|
| Genotype | 2.302 | 1 | 2.30205 | 14.95 | 0.0002 |
| Mitochondria Morphology | 0.8417 | 1 | 0.84172 | 5.47 | 0.0205 |
| Genotype * Mitochondria Morphology | 0.1612 | 1 | 0.16122 | 1.05 | 0.3075 |
| Error | 27.5567 | 179 | 0.15395 | | |
| Total | 29.962 | 182 | | | |

**B** Genotype x Mitochondria Morphology - Spine Volume

| Source | Sum Sq. | d.f. | Mean Sq. | F | Prob>F |
|---|---|---|---|---|---|
| Genotype | 8.518 | 1 | 8.51767 | 16.56 | 0.0001 |
| Mitochondria Morphology | 1.324 | 1 | 1.32404 | 2.57 | 0.1103 |
| Genotype * Mitochondria Morphology | 0.107 | 1 | 0.10681 | 0.21 | 0.6491 |
| Error | 92.043 | 179 | 0.51421 | | |
| Total | 101.097 | 182 | | | |

**C** Genotype x Mitochondria Morphology - PSD Area

| Source | Sum Sq. | d.f. | Mean Sq. | F | Prob>F |
|---|---|---|---|---|---|
| Genotype | 1.3904 | 1 | 1.3904 | 4.86 | 0.0287 |
| Mitochondria Morphology | 0.1623 | 1 | 0.16226 | 0.57 | 0.4523 |
| Genotype * Mitochondria Morphology | 0.0256 | 1 | 0.02556 | 0.09 | 0.7653 |
| Error | 51.1944 | 179 | 0.286 | | |
| Total | 52.6636 | 182 | | | |

**Table 4: 2x2 Factorial ANOVA output tables for Genotype x Mitochondria Morphology.** ANOVA results examining ultrastructural features for synapses containing mitochondria: bouton volume (A), spine volume (B), PSD area (C). All sum of square values shown as constrained (Type III) sum of squares.

***Group Differences in VGLUT2 Particle Size***

To study thalamostriatal axon terminals within the dorsolateral striatum, confocal microscopy and immunofluorescent techniques were used to visualize the density and distribution of VGLUT2 (Fig. 15, 16) and mHTT (Fig. 18), with the addition of colocalization studies to understand where VGLUT2 is colocalized with mHTT (Fig. 19). These studies were performed on three wildtype and three $Q175^{+/-}$ animals. For each animal, tissue sections were chosen at three levels of the striatum: rostral, middle, and caudal. The distribution of VGLUT2+ particles can be seen at all three levels for wildtype (Fig. 15) and $Q175^{+/-}$ mice (Fig. 16). For each tissue, particle analysis was done. An overall examination of binned frequency distribution of VGLUT2+ immunolabeled particles in wildtype and $Q175^{+/-}$ mice reveals significant between-species differences in bin 1 (wildtype: $15.64 \pm 0.15\ \mu m^2$, $Q175^{+/-}$: $17.01 \pm 0.08\ \mu m^2$; $p = 3.41 \times 10^{-22}$; Fig. 17). Comparison of the cumulative frequency between wildtype and $Q175^{+/-}$ VGLUT2+ particle size shows a significant leftward shift in the cumulative distribution of $Q175^{+/-}$ VGLUT2+ particles relative to wildtype VGLUT2+ particles (Kolmogorov-Smirnov test, $p = 1.78 \times 10^{-12}$), demonstrating a higher frequency of smaller VGLUT2+ particles in $Q175^{+/-}$ sections.

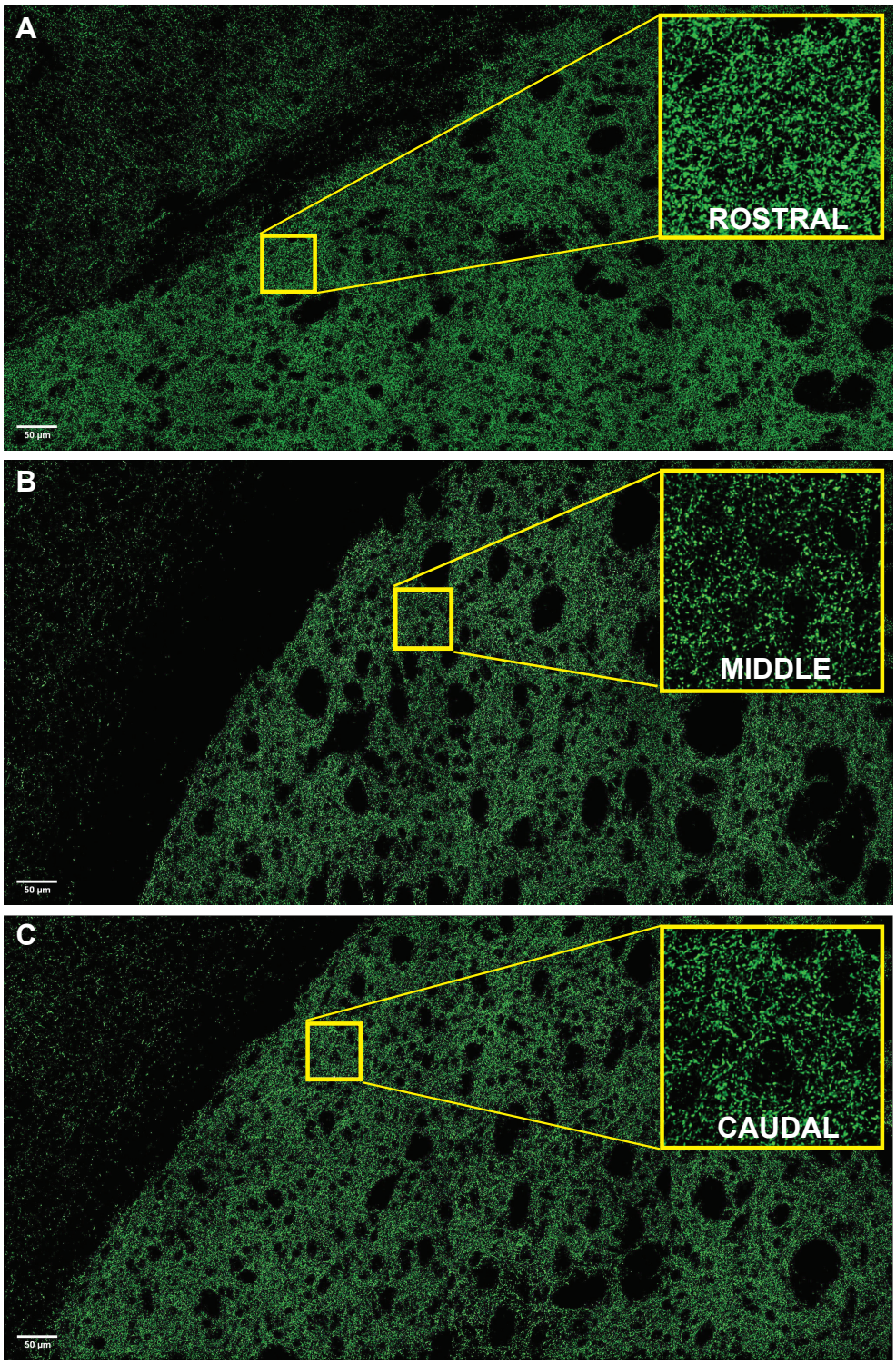


**Figure 15: Wildtype striatal neuropil immunostained for VGLUT2**. Wildtype sections at the rostral (A), middle (B), and caudal (C) levels of the dorsolateral striatum immunolabelled for VGLUT2 (green). Scale bar: 50 microns

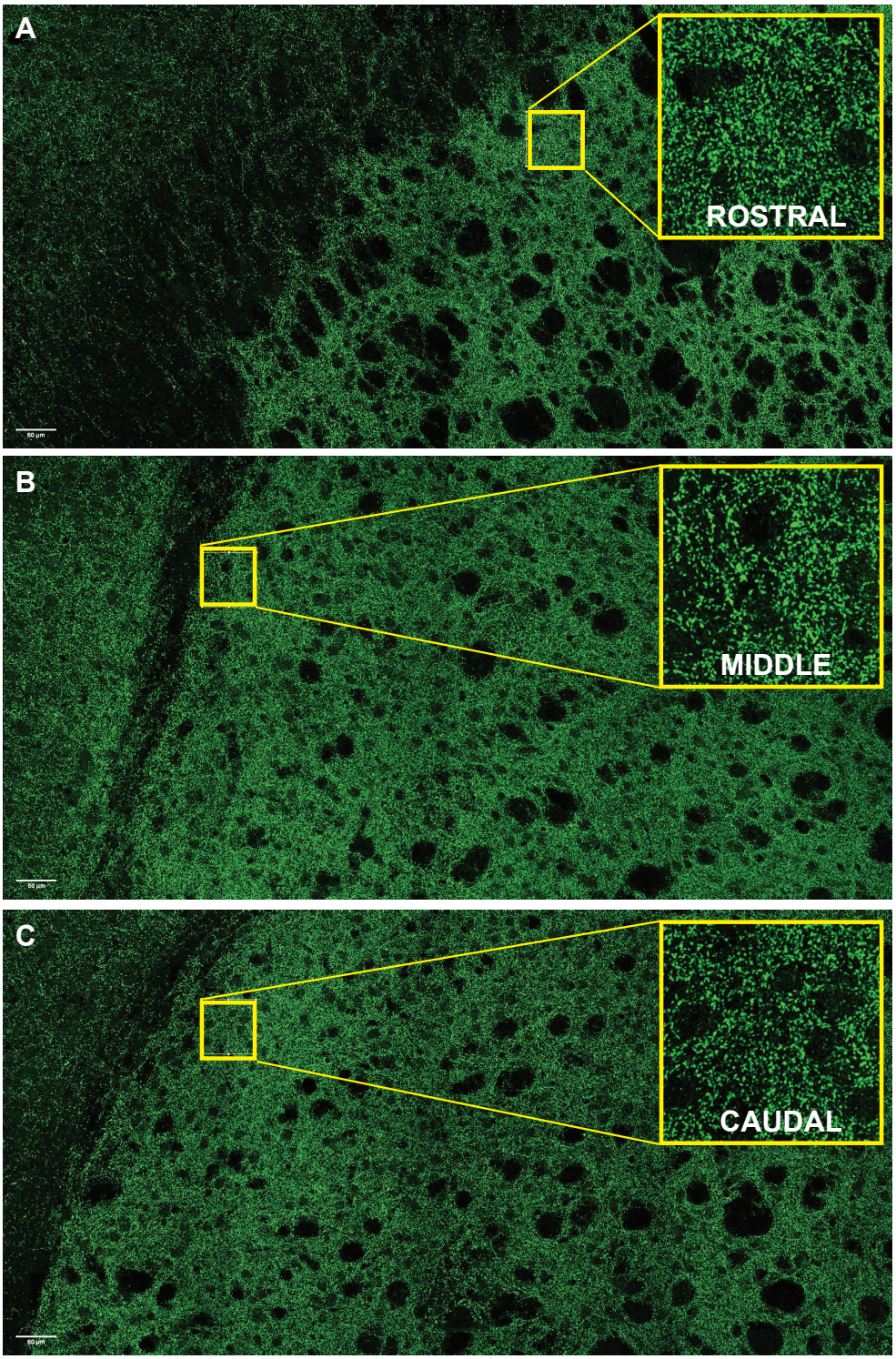


**Figure 16: Q175 striatal neuropil immunostained for VGLUT2**. Q175 sections at the rostral (A), middle (B), and caudal (C) levels of the dorsolateral striatum immunolabelled for VGLUT2 (green). Scale bar: 50 microns

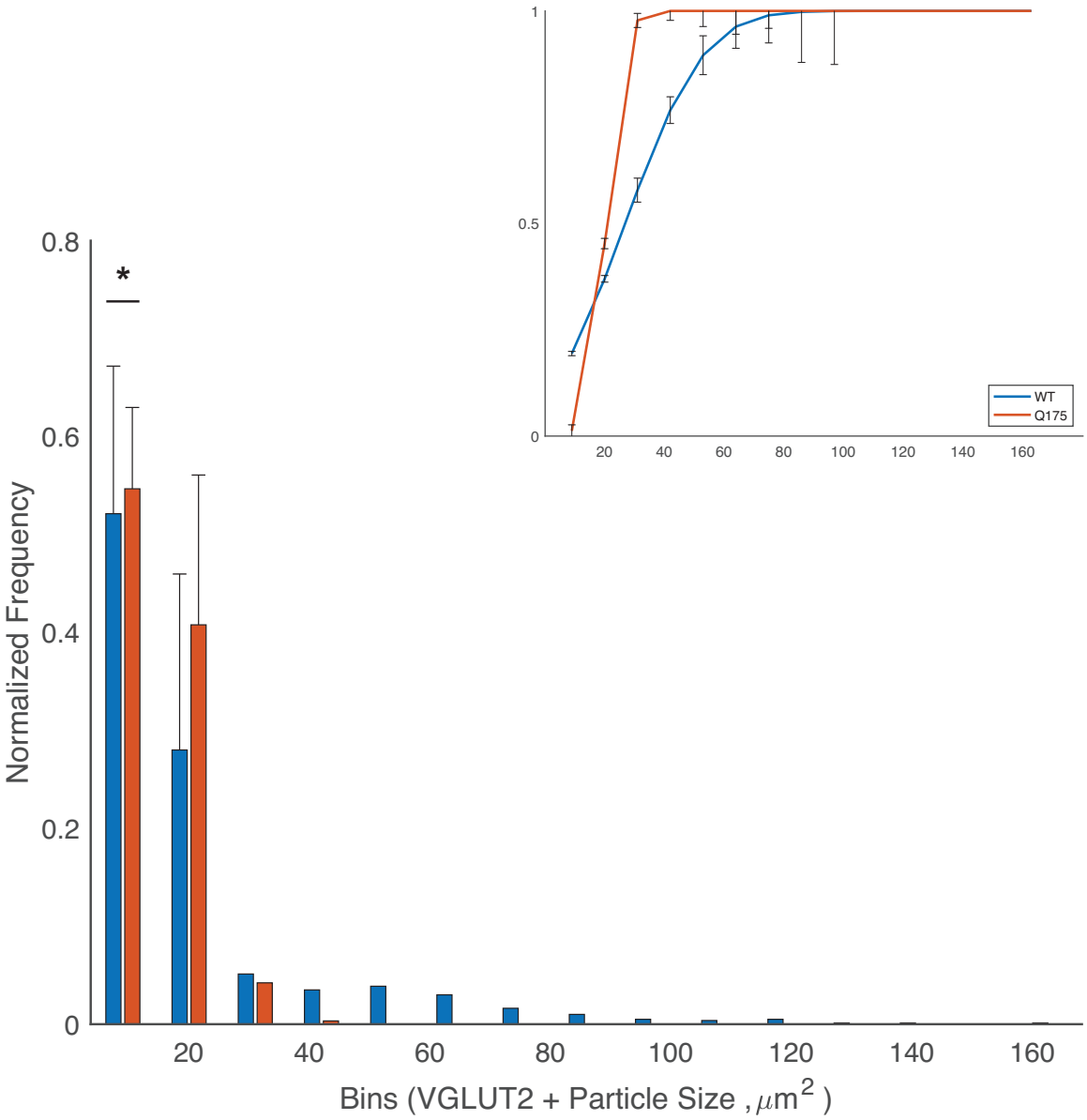


**Figure 17: Distribution of VGLUT2+ particle size.** Relative frequency (main) and cumulative distribution (upper right) based on binned measurements of VGLUT2+ labelled particles in the dorsolateral striatum. * $p < 0.05$

***Regional Differences in VGLUT2, mHTT & Colocalized Particle Density***

To investigate whether there are regional differences in the distribution of VGLUT and mHTT in the dorsolateral striatum, particle analysis was performed at rostral, middle, and caudal level of the striatum to determine the fractional area occupied by VGLUT2+ and mHTT+ particles, as well as dual labelled VGLUT2+/mHTT+ particles. When all VGLUT2+ particles were compared, no significant differences in density were observed between wildtype and $Q175^{+/-}$ sections. Looking closer at the regional distribution of VGLUT2 in the dorsolateral striatum, comparisons between wildtype and $Q175^{+/-}$ VGLUT2+ particle density show that there are significant between-species difference at the rostral (wildtype: $36.92 \pm 2.16\ \mu m^2$, $Q175^{+/-}$: $25.20 \pm 0.55\ \mu m^2$; $p = 0.001$) and middle (wildtype: $11.93 \pm 0.38\ \mu m^2$, $Q175^{+/-}$: $15.17 \pm 0.24\ \mu m^2$; $p = 0.025$) levels of the dorsolateral striatum (Fig. 20A). There were no between-group differences of VGLUT2+ density at the caudal level (wildtype: $13.64 \pm 0.43\ \mu m^2$, $Q175^{+/-}$: $16.30 \pm 0.33\ \mu m^2$). Comparison of VGLUT2+ density between the rostral and middle levels revealed significant within-species differences (wildtype: $p = 7.39 \times 10^{-5}$; $Q175^{+/-}$: $p = 2.40 \times 10^{-5}$). Comparisons between the rostral and caudal also revealed significant within-species differences (wildtype: $p = 9.73 \times 10^{-5}$; $Q175^{+/-}$: $p = 1.32 \times 10^{-4}$). However, no within-group differences of VGLUT2+ density were observed between the middle and caudal levels for either group (wildtype and $Q175^{+/-}$: $p > 0.05$). Collectively, the variability in VGLUT2+

density in wildtype and $Q175^{+/-}$ along the rostral-caudal axis of the dorsolateral striatum suggests that in the normal rodent striatum, VGLUT2 is disproportionately distributed rostrally where there is a higher density.

Comparisons of mHTT+ particle density within $Q175^{+/-}$ tissue sections (Fig. 20) also demonstrate inter-areal differences in mHTT+ particle density along the rostral-caudal axis of the striatum (Fig. 20B), with the smallest average particle density rostrally ($2.54 \pm 0.04\ \mu m^2$), larger density in middle sections ($3.68 \pm 0.11\ \mu m^2$) and highest density caudally ($5.98 \pm 0.91\ \mu m^2$). A significant areal difference in mHTT+ density was only seen when comparing the rostral and middle levels of the striatum ($p = 0.003$). All other areal comparisons were non-significant (rostral and caudal: $p > 0.05$; middle and caudal: $p > 0.05$). Particles positively labelled for both VGLUT2 and mHTT underwent colocalization analysis (Fig. 19). Areal comparisons of VGLUT2+ / mHTT+ particle density suggest that observed regional differences in dual labeled particle density are not significantly different (all $p > 0.05$) in the dorsolateral striatum (Fig. 20C).

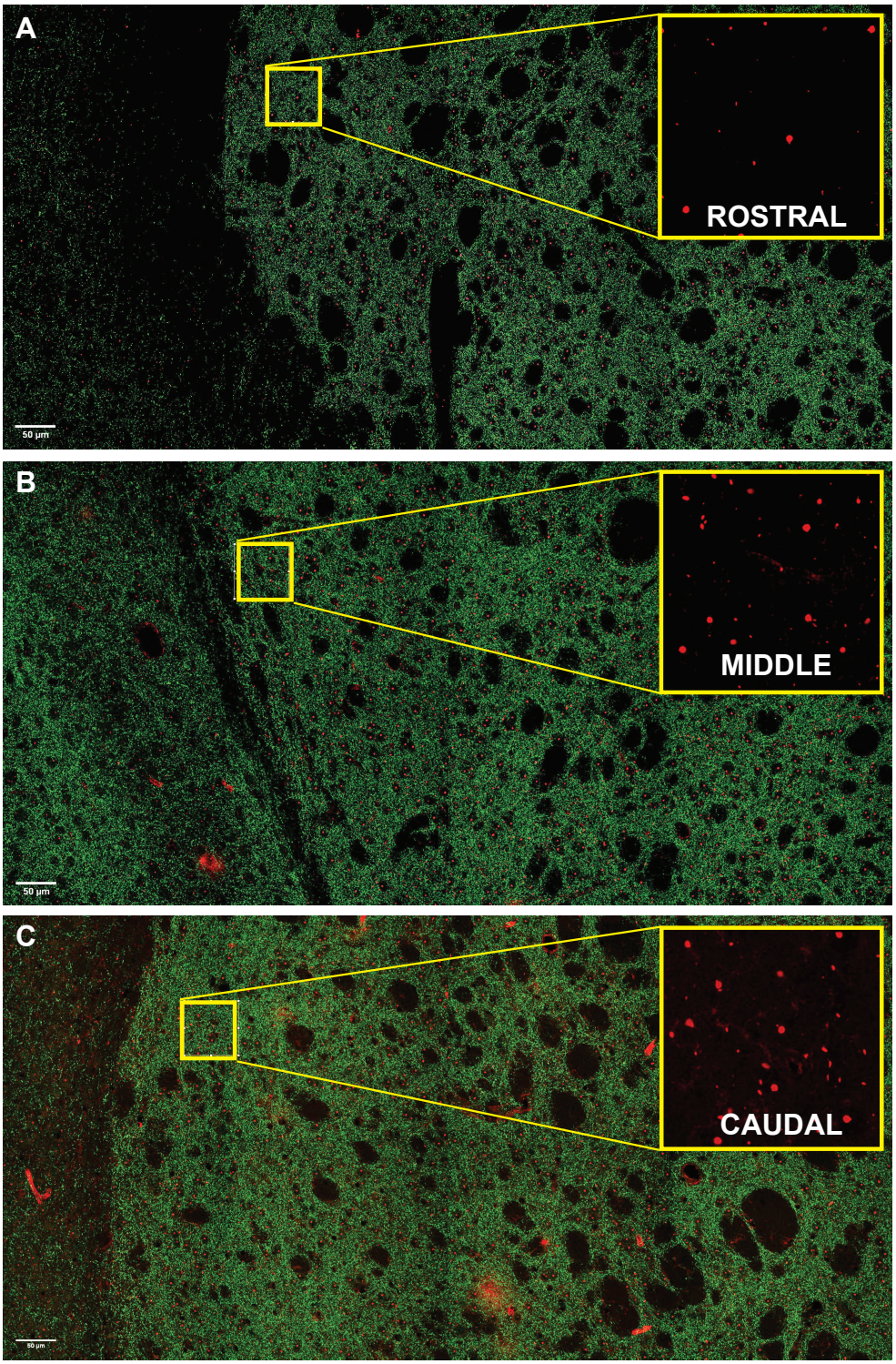


**Figure 18: Q175 striatal neuropil immunostained for mHTT**. Q175 sections at the rostral (A), middle (B), and caudal (C) levels of the dorsolateral striatum immunolabelled for mHTT (red). Scale bar: 50 microns

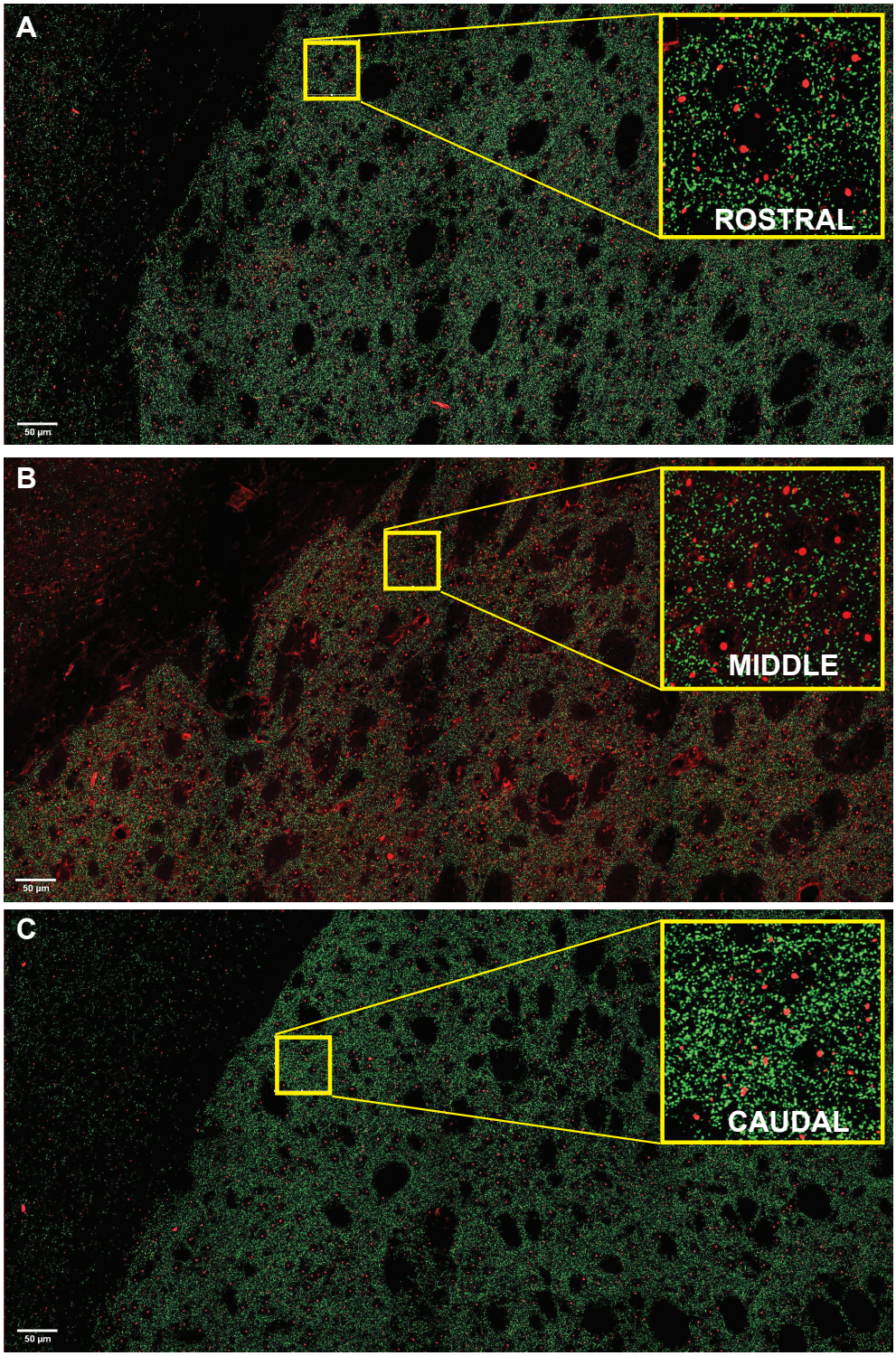


**Figure 19: Q175 striatal neuropil immunostained for VGLUT2 & mHTT**. Q175 sections at the rostral (A), middle (B), and caudal (C) levels of the dorsolateral striatum immunolabelled for VGLUT2 (green) and mHTT (red). Scale bar: 50 microns

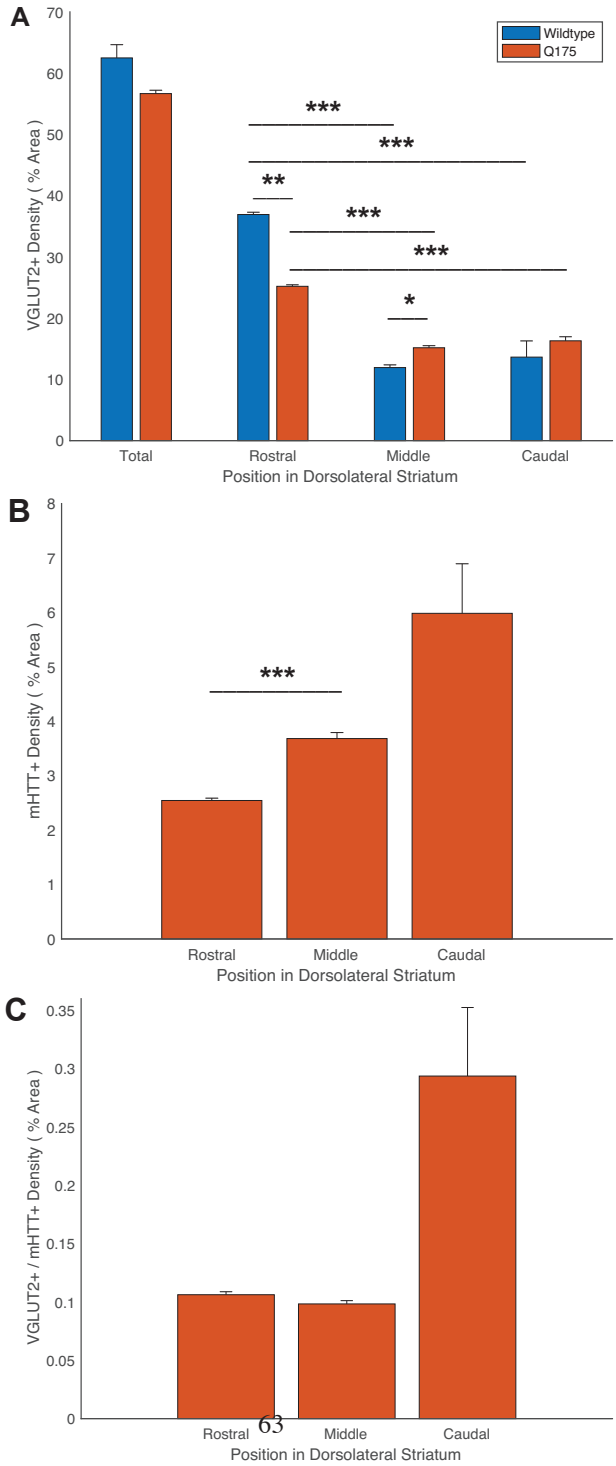


**Figure 20: Density of VGLUT2, mHTT, & VGLUT2 / mHTT colocalized particles.** Fractional area of VGLUT2+ (A), mHTT+ (B), and VGLUT2+ / mHTT+ (C) particles along the rostral-caudal axis of the dorsolateral striatum. * $p < 0.05$; ** $p < 0.005$; *** $p < 0.0005$

## DISCUSSION

From the earliest studies of the HD brain, the progressive thinning of the striatum and cerebral cortex are prominent pathological events of disease progression (Vonsattel & DiFiglia, 1998). Atrophy in these regions have consequences on a neuronal and a circuit level due the loss of neurons within the respective brain regions. The degeneration of MSNs in the striatum leads to alterations in glutamate neurotransmission and may underlie early motor abnormalities such as chorea in symptomatic HD individuals (NINDS, 1998). These observations and their detrimental consequences highlight the need to understand how the presence of mHTT may affect the structure of the synaptic circuitry in the dorsolateral striatum at multiple levels. At the ultrastructural level, our data recapitulates differences in pre-synaptic and post-synaptic features seen among VGLUT2+ axospinous synapses (Deng et al., 2013; Deng et al., 2014) and thalamostriatal input loss to the dorsal striatum (Deng et al., 2013; Deng et al., 2014; Parievsky et al., 2017), and further characterizes general synapse characteristics and thalamostriatal input loss to the dorsal striatum. An in-depth examination of the influence of genotype, the presence or absence of VGLUT2, and mitochondria morphology as distinct categorical variables demonstrates the multivariate relationships between each variable and ultrastructural feature. At the microcircuit level, our data provides novel insights into the size, density and distribution of VGLUT2+ and mHTT+ immunolabelled particles along the rostral-caudal axis of the dorsolateral striatum. Collectively, the findings from this study offer insights into how the presence of mHTT impair synaptic transmission at the neuronal and circuit level.

General characteristics of VGLUT2+ and VGLUT2- synapses in $Q175^{+/-}$ animals demonstrate an uneven ratio of macular to perforated synapses in $Q175^{+/-}$ animals, with 79% of VGLUT2+ synapses and 63% of VGLUT2- synapses being macular. In wildtype mice, the ratio of macular to perforated synapses is lower, with 59% of VGLUT2+ synapses and 54% of VGLUT2- synapses being macular. The disproportionately higher ratio of macular to perforated synapses seen among $Q175^{+/-}$ mice in both VGLUT2+ and VGLUT2- synapses suggests a shift away from long term potentiation (LTP) of glutamate at the synapse, since LTP is positively associated with axospinous synapses that have more perforated PSDs, and more perforated axospinous synapses in general (Dhanrajan et al., 2004; Geinisman, deToledo-Morrell, & Morrell, 1991; Geinisman et al., 1993). From this observation, we would expect to find fewer multi-synaptic boutons (MSBs) within $Q175^{+/-}$ synapses. However, the number of MSBs remained the same, making up 20-25% of all pre-synaptic boutons across wildtype and $Q175^{+/-}$ synapses.

Quantitative assessments of synapse size were performed on two pre-synaptic features and two post-synaptic features. Assessments of pre-synaptic bouton volume reveal no significant differences between wildtype and $Q175^{+/-}$ for both VGLUT2+ and VGLUT2- axospinous synapses. Our findings follow a similar trend observed by similar pre-synaptic cross-sectional measurements of terminal diameter and terminal area among VGLUT2+ wildtype and Q140 axospinous synapses (Deng et al., 2013; Deng et al., 2014). However, a similar study in age matched R6/2 mice displayed a significant decrease in

VGLUT2+ axospinous synapses with D1R- expressing dendritic spines (Parievsky et al., 2017). Among all VGLUT2+ synapses, mitochondria present in $Q175^{+/-}$ pre-synaptic boutons demonstrate a significant lower volume compared to wildtype. Examination of morphology reveals a ~3:1 ratio of damaged to normal mitochondria, as 65% of VGLUT2+ synapses and 71% of VGLUT2- synapses contained damaged mitochondria. Within these mitochondria, evidence of mitochondrial fission and abnormal elongation was found in $Q175^{+/-}$ mice, consistent with observations from previous HD studies (Costa et al., 2010; Song et al., 2011). Wildtype and $Q175^{+/-}$ VGLUT2- pre-synaptic features were comparable but non-significant.

Comparisons of post-synaptic spine volume and the area occupied by the PSD at the synaptic junction (PSD area) both demonstrated significant differences between wildtype and $Q175^{+/-}$ VGLUT2+ synapses. Notably, the average spine volume in wildtype animals was approximately two times larger than the average $Q175^{+/-}$ spine, contrasting to spine volume measurements from in wildtype and $Q175^{+/-}$ VGLUT2- synapses which were relatively similar. The cumulative distribution of spine volumes in VGLUT2+ synapses reveal a significant leftward shift, indicating that a higher frequency of smaller spines was seen in $Q175^{+/-}$ neuropil. Reductions in spine size have also been observed among thalamostriatal axospinous synapses with D1R- and D2R- labelled spines in Q140 mice, but only D1R- spines showed a significant decrease in cross-sectional spine area relative to wildtype (Deng et al., 2014). The average PSD area was also significantly different

among VGLUT2+ synapses, with reductions observed among $Q175^{+/-}$ synapses relative to wildtype. No significant differences were seen between wildtype and $Q175^{+/-}$ mice for any VGLUT2- synaptic features. The density of $Q175^{+/-}$ VGLUT2+ synapses among all 3D reconstructed synapses was reduced two-fold compared to wildtype synapses. This was observed among $Q175^{+/-}$ VGLUT2- synapses as well. Separate correlation analyses among pre- and post-synaptic features of wildtype and $Q175^{+/-}$ synapses show that the only significant correlations were observed between PSD area and post-synaptic spine volume in VGLUT2+ and VGLUT2- wildtype synapses, suggesting that pre- and post-synaptic ultrastructural features may not be linearly or causally related in $Q175^{+/-}$ VGLUT2+ and VGLUT2- axospinous synapses.

To understand the specific influence of genotype and synaptic input (presence or absence of VGLUT2) categorical type on synaptic and mitochondrial ultrastructural features (volume and damage), we used multivariate comparisons of our outcome measures. When comparisons were made for ultrastructural features from all synapses, genotype was not a significant main effect for any features. However, after excluding the features from synapses without mitochondria, genotype was a significant main effect for pre-synaptic bouton volume, pre-synaptic mitochondria volume and post-synaptic spine volume. Comparisons of genotype and mitochondria morphology (normal or abnormal) categorical types on ultrastructural features from the same group of synapses reveals that genotype was a significant main effect for pre-synaptic bouton volume, post-synaptic spine

volume and PSD area. These results suggest that the presence of mHTT (genotype) is a reliable predictor of pre- and post-synaptic ultrastructural features the presence of mHTT (genotype) coupled with observations of mitochondria morphology may be a better predictor of observed reductions in the area of synapse of the PSD at the synaptic junction among axospinous synapses containing mitochondria. Further studies are needed to determine the significant interactions between the categorical variables in these comparisons.

Considering our analyses examining the relationships between numerous categorical variables and the observations of reduced mitochondria size and aberrant morphology, our results suggests that the mHTT may be altering the synaptic properties observed among thalamostriatal axospinous synapses in a cell autonomous manner by affecting normal mitochondria function. However, further characterization of mHTT proteins at the ultrastructural level is required to determine this causal relationship. The comparisons described above may also explain why a linear relationship between pre-synaptic bouton volume and PSD area was only observed among wildtype synapses, but not for $Q175^{+/-}$ synapses. Together our results corroborate and support the notion that differences observed between wildtype and $Q175^{+/-}$ axospinous synapses may be non-linearly influenced by levels of various synaptic categorical variables.

Confocal studies of the dorsolateral striatum demonstrate that there are no significant losses to thalamostriatal inputs to the dorsolateral striatum between wildtype and $Q175^{+/-}$ mice at 12-months, corroborating a previous study from our lab. However, in-depth analyses of

VGLUT2 distribution suggests that VGLUT2 is not uniform along the rostral-caudal axis of the dorsolateral striatum. This observation was seen among both wildtype and $Q175^{+/-}$ mice. VGLUT2 was disproportionately distributed rostrally where there was a higher density, while a lower density was found caudally. The cumulative distribution of VGLUT2+ particle size reveals a significant leftward shift, indicating that a higher frequency of smaller particles was seen among $Q175^{+/-}$ synapses. Both between-group and regional comparisons of VGLUT2 density distribution demonstrates that the presence of a topographical distribution of VGLUT2 along the rostral-caudal axis. Within-group comparisons for $Q175^{+/-}$ sections demonstrates that the distribution of mHTT is inversed, as there was a lower density of mHTT rostrally and a higher density caudally. This observation remained true for particles double labelled for VGLUT2 and mHTT.

Observations from our confocal studies support the pattern of early motor deficits observed among symptomatic HD individuals (NINDS, 1998). Functional distinctions along the rostral-caudal axis suggest that the rostral end of the dorsal striatum receives glutamatergic projections from the frontal and parietal cortical areas, while the caudal receives projections from the primary motor and somatosensory cortices (Ferré et al., 2018). Within the thalamus, one study found that input from thalamic intralaminar nuclei in the parafascicular (parafascicular, posterior, and centrolateral nuclei) and the ventroposterior (ventroposteromedial, ventromedial, and ventroposterolateral nuclei) regions of the thalamus are the main inputs to the dorsomedial and dorsolateral striatum respectively and that these thalamostriatal projections contribute to the smooth initiation

of movement, with ventroposterior nuclei specifically influencing the motor execution of learned motor actions (Díaz-Hernández et al., 2018). Though this study doesn't specify the regional contributions of these projections along the rostral-caudal axis in the striatum, studies of the MSNs projecting to the caudal rodent striatum suggest that the caudal regions of the cerebral cortex and the thalamus as the main projections to the caudal striatum (Jiang & Kim, 2018). Collectively, these findings suggest that glutamatergic projections from ventral motor thalamic nuclei and caudal intralaminar nuclei from the centromedian-parafascicular nuclear complex are the main contributors of thalamic motor input to the caudal level of the dorsal striatum. Our confocal studies, which suggest a significant reduction in VGLUT2+ axon terminals at the caudal level of the dorsolateral striatum supports these anatomical distinctions and is in line with observed motor deficits at the symptomatic stage of HD.

The results of this study demonstrate that the presence of mHTT may be altering the synaptic circuitry at the ultrastructural and microcircuit levels in the $Q175^{+/-}$ model mice. At the ultrastructural level, the findings of our study recapitulate observations of the influence that mHTT may have on pre- and post-synaptic elements of VGLUT2+ axospinous synapses (Deng et al., 2013; Deng et al., 2014; Parievsky et al., 2017). Pre-synaptically, we observed a preservation of axon terminal size, but reductions in mitochondria size and aberrant mitochondria morphology in pre-synaptic boutons. We also observed a two-fold reduction in post-synaptic spine volume, in addition to reduced synapse area at the synaptic junction. Overall, a 50% reduction in thalamostriatal axospinous synapse abundance was observed. There were marked differences in our results

when compared to previous ultrastructural studies (Deng et al., 2013; Deng et al., 2014; Parievsky et al., 2017). The most likely explanation for the observed differences is the specific mouse model used in each study, as the Q140 and R6/2 models contain 140 and 144 polyQ repeats respectively (Mangiarini et al., 1996; Menalled et al., 2012), while the $Q175^{+/-}$ model used in the current study contains 188 polyQ repeats (Menalled et al., 2012). Interestingly enough, considering the inverse relationship with length of polyQ repeats leads to earlier disease severity (HDCRG, 1993), we expected to find a greater loss of thalamostriatal terminals at 12-months. This was not the case as only a 50% reduction was observed. These differences can be attributed to numerous factors such as methodology, experimental design, and counting methods. For example, the referenced ultrastructural studies utilized 2D methods as pre- and post-synaptic measurements were derived from cross sectional area (Deng et al., 2013; Deng et al., 2014; Parievsky et al., 2017) while our measurements were derived from volumetric features from 3D reconstructed synaptic elements. Additionally, the R6/2 study did not use stereological methods in their quantification of synapse density so their results may be an underestimation of synapse loss in the dorsolateral striatum (Parievsky et al., 2017). Despite these differences, our results are in general agreement with the idea that the presence of mHTT has a larger impact on post-synaptic elements of VGLUT2+ axospinous synapses than pre-synaptic elements in the brains of symptomatic HD mouse models.

In the current study, D1- and D2- expressing MSNs were not labelled – both our ultrastructural and confocal microscopy studies identified VGLU2+ labelled axon terminals. Studies of VGLUT1+ and VGLUT2+ excitatory glutamatergic terminals at the

microcircuit level found that all axon terminals were located within 1 μm of a dopaminergic synapse, suggesting that MSNs synapses receiving excitatory afferents share the same structural relationships as MSNs modulated by DA (Moss & Bolam, 2008). Applying this relationship, our findings of a rostral-to-caudal reduction in VGLUT2 density suggests that a similar observation among VGLUT2 axon terminals synapsing onto D1- and D2-expressing spines might be observed. However, human imaging studies and a rodent study using immunohistochemical methods examining the distribution of D1- and D2- receptor in the dorsal striatum found that the density of D1- receptor expression along the rostral-caudal axis was decreased in the putamen while not in the caudate nuclei, but D2- receptor expression increasing along the rostral-caudal axis for both nuclei (Piggott et al., 1999). The rodent study found that D2- receptor expression along the same axis was decreased in the caudate nuclei, contrasting to the previous study (Levey et al., 1993). Previously, our lab described significant functional changes in D1- receptor expressing MSNs and not D2-MSNs in the $Q175^{+/-}$ HD model (Goodliffe et al., 2018). The distribution of D1- and D2-MSNs along the rostral-caudal axis has not been extensively studied. However, one study found that D2 receptor expression was lower in a specific caudal region of the mouse striatum where a high expression of D1 receptors were found, but otherwise found that the distribution of D1 and D2 receptor expression was random in the dorsal striatum (Gangarossa et al., 2013). Further studies are needed to determine if there are regional differences in D1- and D2- receptor expression along the rostral-caudal axis and whether the differences support distinct functions of the specific thalamostriatal inputs at each level. Only then can a pathway- and region-specific relationship be formulated.

The current study of thalamostriatal afferents to the striatum only tells half of the story of the effect that mHTT presence may have on glutamate neurotransmission. The other half of the story involves excitatory corticostriatal afferents. Further studies of corticostriatal input loss and characterization of VGLUT1+ axospinous synapses in symptomatic HD mice (12-months) at the ultrastructural level will provide insight to the global excitatory: inhibitory imbalance occurring along the rostral-caudal axis of the dorsolateral striatum. However, the results of this study demonstrate a 50% reduction in VGLUT2+ axospinous synapses in $Q175^{+/-}$ animals at an ultrastructural level. At the microcircuit level, a significant 32% reduction (overall 9.7% reduction) of VGLUT2+ spatial abundance within rostral regions of the dorsolateral striatum. It is important to remember that the results from our confocal studies do not differentiate between axospinous and axodendritic axon terminals. However, studying the synaptic alterations at both levels suggest that the presence of mHTT may contribute to both cell-autonomous mechanisms as seen on the ultrastructural level, and possibly non-cell autonomous mechanisms that may affect the larger local striatal synaptic circuit. A loss of excitatory glutamatergic inputs to the striatum continue to further corroborates the idea that an excitatory: inhibitory imbalance may contribute to structural synaptic changes. However, further studies are needed to determine the way that these mechanisms may affect synaptic transmission at the functional level.

## REFERENCES


Allen Institute for Brain Science. (2011). Allen Mouse Brain Connectivity Atlas. http://connectivity.brain-map.org/

Andrew, S. E., Goldberg, Y. P., Kremer, B., Telenius, H., Theilmann, J., Adam, S., . . . Hayden, M. R. (1993). The relationship between trinucleotide (CAG) repeat length and clinical features of Huntington's disease. *Nature Genetics, 4*(4), 398 403. doi:10.1038/ng0893-398

Bates, G. P., Dorsey, R., Gusella, J. F., Hayden, M. R., Kay, C., Leavitt, B. R., . . . Tabrizi, S. J. (2015). Huntington disease. *Nature Reviews Disease Primers, 1*(1). doi:10.1038/nrdp.2015.5

Bates, G. (1997). Transgenic models of Huntington's disease. *Human Molecular Genetics, 6*(10), 1633-1637. doi:10.1093/hmg/6.10.1633

Bence, N. F., Sampat, R. M., & Kopito, R. R. (2001). Impairment of the ubiquitin-proteasome system by protein aggregation. *Science (New York, N.Y.)*, *292*(5521), 1552–1555. doi:10.1126/science.292.5521.1552

BioRender. (2020). Direct and Indirect Pathways of the Basal Ganglia. Link: https://bit.ly/38gXnno

Blomeley, C. P., Kehoe, L. A., & Bracci, E. (2009). Substance P Mediates Excitatory Interactions between Striatal Projection Neurons. *Journal of Neuroscience, 29*(15), 4953-4963. doi:10.1523/jneurosci.6020-08.2009

Bruzelius, E., Scarpa, J., Zhao, Y., Basu, S., Faghmous, J. H., & Baum, A. (2019). Huntington's disease in the United States: Variation by demographic and

socioeconomic factors. *Movement Disorders, 34*(6), 858-865. doi:10.1002/mds.27653

Cattaneo, E., Zuccato, C., & Tartari, M. (2005). Normal huntingtin function: An alternative approach to Huntington's disease. *Nature Reviews Neuroscience, 6*(12), 919-930. doi:10.1038/nrn1806

Chakravarthy, V. S., Joseph, D., & Bapi, R. S. (2010). What do the basal ganglia do? A modeling perspective. *Biological Cybernetics, 103*(3), 237-253. doi:10.1007/s00422-010-0401-y

Chen, Z., Jalabi, W., Hu, W., Park, H., Gale, J. T., Kidd, G. J., . . . Trapp, B. D. (2014). Microglial displacement of inhibitory synapses provides neuroprotection in the adult brain. *Nature Communications, 5*(1). doi:10.1038/ncomms5486

Chissoe, W.F., Vezey E.L., & John J. Skvarla. (1995) The Use of Osmium Thiocarbohydrazide for Structural Stabilization and Enhancement of Secondary Electron Images in Scanning Electron Microscopy of Pollen. *Grana, 34*(5), 317 324. doi:10.1080/00173139509429065

Colonnier, M., & Beaulieu, C. (1985). An empirical assessment of stereological formulae applied to the counting of synaptic disks in the cerebral cortex. *The Journal of Comparative Neurology, 231*(2), 175-179. doi:10.1002/cne.902310205

Costa, V., Giacomello, M., Hudec, R., Lopreiato, R., Ermak, G., Lim, D., . . . Scorrano, L. (2010). Mitochondrial fission and cristae disruption increase the response of cell models of Huntington's disease to Apoptotic stimuli. *EMBO Molecular Medicine, 2*(12), 490-503. doi:10.1002/emmm.201000102

Craufurd, D., Thompson, J. C., & Snowden, J. S. (2001). Behavioral changes in Huntington Disease. *Neuropsychiatry neuropsychology, and behavioral neurology, 14*(4), 219-226.

Cummings, D. M., Alaghband, Y., Hickey, M. A., Joshi, P. R., Hong, S. C., Zhu, C., . . . Levine, M.S. (2012). A critical window of Cag repeat-length correlates with Phenotype severity in the R6/2 mouse model of Huntington's disease. *Journal of Neurophysiology, 107*(2), 677-691. doi:10.1152/jn.00762.2011

Davies, S. W., Turmaine, M., Cozens, B. A., DiFiglia, M., Sharp, A. H., Ross, C. A., . . . Bates, G. P. (1997). Formation of neuronal intranuclear inclusions underlies the neurological dysfunction in mice transgenic for the hd mutation. *Cell, 90*(3), 537 548. doi:10.1016/-s0092-8674(00)80513-9

Deng, Y., Albin, R., Penney, J., Young, A., Anderson, K., & Reiner, A. (2004). Differential loss of striatal projection systems in Huntington's disease: A quantitative immune histochemical study. *Journal of Chemical Neuroanatomy, 27*(3), 143-164. doi:10.1016/-j.jchemneu.2004.02.005

Deng, Y., Wong, T., Bricker-Anthony, C., Deng, B., & Reiner, A. (2013). Loss of Corticostriatal and Thalamostriatal Synaptic Terminals Precedes Striatal Projection Neuron Pathology in Heterozygous Q140 Huntington's Disease Mice. *Neurobiology of Disease, 60*, 89-107. doi:10.1016/j.nbd.2013.08.009

Deng, Y., Wong, T., Wan, J. Y., & Reiner, A. (2014). Differential loss of Thalamostriatal and corticostriatal input to Striatal projection neuron types prior to overt motor

symptoms in the Q140 Knock-in mouse model of Huntington's disease. *Frontiers in Systems Neuroscience, 8*. doi:10.3389/fnsys.2014.00198

Dhanrajan, T. M., Lynch, M. A., Kelly, A., Popov, V. I., Rusakov, D. A., & Stewart, M. (2004). Expression of long-term potentiation in aged rats involves perforated synapses but dendritic spine branching results from high-frequency stimulation alone. *Hippocampus, 14*(2), 255-264. doi:10.1002/hipo.10172

Díaz-Hernández, E., Contreras-López, R., Sánchez-Fuentes, A., Rodríguez-Sibrían, L., Ramírez Jarquín, J. O., & Tecuapetla, F. (2018). The Thalamostriatal Projections contribute to the initiation and execution of a sequence of movements. *Neuron, 100*(3). doi:10.1016/j.neuron.2018.09.052

DiFiglia, M., Sapp, E., Chase, K. O., Davies, S. W., Bates, G. P., Vonsattel, J. P., & Aronin, N. (1997). Aggregation of huntingtin in neuronal intranuclear inclusions and dystrophic neurites in brain. *Science (New York, N.Y.)*, *277*(5334), 1990 1993.

Ferré, S., Bonaventura, J., Zhu, W., Hatcher-Solis, C., Taura, J., Quiroz, C., Zwilling, D. (2018). Essential control of the function of The striatopallidal neuron By Pre Coupled complexes of Adenosine a2a-dopamine D2 receptor heterotetramers and Adenylyl Cyclase. *Frontiers in Pharmacology, 9*. doi:10.3389/fphar.2018.00243

Fiala, J. C., & Harris, K. M. (2001). Extending Unbiased Stereology of Brain

Ultrastructure to Three-dimensional Volumes. *Journal of the American Medical Informatics Association, 8*(1), 1-16. doi:10.1136/jamia.2001.0080001

Fix, J. D. (2008). Basal Ganglia and the Striatal Motor System. In *Neuroanatomy* (pp. 274-281). Philadelphia: Wolters Kluwer/Lippincott Williams & Wilkins

Fremeau, R. T., Troyer, M. D., Pahner, I., Nygaard, G. O., Tran, C. H., Reimer, R. J., . . . Edwards, R. H. (2001). The expression of vesicular glutamate transporters defines two classes of excitatory synapse. *Neuron, 31*(2), 247-260. doi:10.1016/s0896 6273(01)003440

Fujiyama, F., Kuramoto, E., Okamoto, K., Hioki, H., Furuta, T., Zhou, L., . . . Kaneko, T. (2004).Presynaptic localization of An AMPA-type glutamate receptor In Corticostriatal and Thalamostriatal axon terminals. *European Journal of Neuroscience, 20*(12), 3322-3330. doi:10.1111/j.1460-9568.2004.03807.x

Galvan, A., & Smith, Y. (2014). Basal Ganglia. In *Encyclopedia of the Neurological Sciences* (2nd ed., pp. 387-392). Waltham, MA: Academic Press/Elsevier. doi:10.1016/B978-0-12-385157-4.01118-0

Gangarossa, G., Espallergues, J., Mailly, P., De Bundel, D., De Kerchove d'Exaerde, A., Hervé, D., ... Krieger, P. (2013). Spatial distribution of d1r- and d2r-expressing medium-sized spiny neurons differs along the rostro-caudal axis of the mouse dorsal striatum. *Frontiers in Neural Circuits, 7*. doi:10.3389/fncir.2013.00124

Gerfen, C., Engber, T., Mahan, L., Susel, Z., Chase, T., Monsma, F., & Sibley, D. (1990). D1 and D2 dopamine receptor-regulated gene expression of striatonigral and

striatopallidal neurons. *Science, 250*(4986), 1429-1432. doi:10.1126/science.2147780

Gerfen, C., Mcginty, J., & Young, W. (1991). Dopamine differentially regulates dynorphin, substance P, and enkephalin expression in striatal neurons: In situ hybridization histochemical analysis. *The Journal of Neuroscience, 11*(4), 1016 1031. doi:10.1523/jneurosci.11-04-01016.1991

Gerfen, C. R., & Surmeier, D. J. (2011). Modulation of Striatal projection systems by dopamine. *Annual Review of Neuroscience, 34*(1), 441-466. doi:10.1146/annurev-neuro-061010-113641

Goodliffe, J. W., Song, H., Rubakovic, A., Chang, W., Medalla, M., Weaver, C. M., & Luebke, J. I. (2018). Differential changes to D1 and D2 medium spiny neurons in the 12-month-old q175+/- mouse model of Huntington's Disease. *PLoS ONE, 13*(8). doi:10.1371/journal.pone.0200626

Glass, M., Dragunow, M., & Faull, R. (2000). The pattern of neurodegeneration in Huntington's disease: A comparative study of cannabinoid, dopamine, adenosine and GABAA receptor alterations in the human basal ganglia in Huntington's disease. *Neuroscience, 97*(3), 505-519. doi:10.1016/s0306-4522(00)00008-7

Graham, R. K., Deng, Y., Slow, E. J., Haigh, B., Bissada, N., Lu, G., Pearson, J., Shehadeh, J., Bertram, L., Murphy, Z., Warby, S. C., Doty, C. N., Roy, S., Wellington, C. L., Leavitt, B. R., Raymond, L. A., Nicholson, D. W., & Hayden, M. R. (2006). Cleavage at the caspase-6 site is required for neuronal dysfunction and degeneration due to mutant huntingtin. *Cell*, *125*(6), 1179–1191.

doi:10.1016/j.cell.2006.04.026

Graveland, G., & Difiglia, M. (1985). The frequency and distribution of medium-sized neurons with indented nuclei in the primate and rodent neostriatum. *Brain Research, 327*(1-2), 307-311. doi:10.1016/0006-8993(85)91524-0

Gray, M., Shirasaki, D. I., Cepeda, C., Andre, V. M., Wilburn, B., Lu, X., . . . Yang, X. (2008). Full-Length Human Mutant Huntingtin with a Stable Glutamine Repeat can Elicit Progressive and Selective Neuropathogenesis in BACHD Mice. *Journal of Neuroscience, 28*(24), 6182-6195. doi:10.1523/jneurosci.0857-08.2008

Gutekunst, C. A., Li, S. H., Yi, H., Mulroy, J. S., Kuemmerle, S., Jones, R., Rye, D., Ferrante, R. J., Hersch, S. M., & Li, X. J. (1999). Nuclear and neuropil aggregates in Huntington's disease: relationship to neuropathology. *The Journal of neuroscience: the official journal of the Society for Neuroscience*, *19*(7), 2522 2534. doi:10.1523/JNEUROSCI.19-07-02522.1999

Harper, P. S., & Jones, L. (2002). Huntington's disease: Genetic and molecular studies. In G. P. Bates, P. S. Harper, & L. Jones (Eds.), *Huntington's disease* (3rd ed., pp. 113–158). Oxford, UK: Oxford University Press

Herzog, E., Bellenchi, G. C., Gras, C., Bernard, V., Ravassard, P., Bedet, C., . . . El Mestikawy, S. (2001). The existence of a second vesicular glutamate transporter specifies subpopulations of glutamatergic neurons. *The Journal of Neuroscience, 21*(22). doi:10.1523/jneurosci.21-22-j0001.2001

HDCRG. (1993). A novel gene containing a trinucleotide repeat that is expanded and

unstable on Huntington's disease chromosomes. *Cell 72*, 971–983.

Indersmitten, T., Tran, C. H., Cepeda, C., & Levine, M. S. (2015). Altered excitatory and inhibitory inputs to striatal medium-sized spiny neurons and cortical pyramidal neurons in The Q175 mouse model of Huntington's disease. *Journal of Neurophysiology, 113*(7), 2953-2966. doi:10.1152/jn.01056.2014

Jiang, H., & Kim, H. F. (2018). Anatomical inputs from the sensory and value structures to the tail of the rat striatum. *Frontiers in Neuroanatomy, 12*. doi:10.3389/fnana.2018.00030

Kim, J., Moody, J. P., Edgerly, C. K., Bordiuk, O. L., Cormier, K., Smith, K., Ferrante, R.J.

(2010). Mitochondrial loss, dysfunction and Altered dynamics in Huntington's disease. *Human Molecular Genetics, 19*(20), 3919-3935. doi:10.1093/hmg/ddq306

Jiang, H., Nucifora, F. C., Jr, Ross, C. A., & DeFranco, D. B. (2003). Cell death triggered by polyglutamine-expanded huntingtin in a neuronal cell line is associated with degradation of CREB-binding protein. *Human Molecular Genetics, 12*(1), 1–12. doi:10.1093/hmg/ddg002

Hsu, A., Luebke, J. I., & Medalla, M. (2017). Comparative ultrastructural features of excitatory synapses in the visual and frontal cortices of the adult mouse and monkey. *Journal of Comparative Neurology, 525*(9), 2175-2191. doi:10.1002/cne.24196

Hughes, A. & Jones, L. in *Huntington's Disease* (eds Bates, G. P., Tabrizi, S. J. & Jones,

L.) 323–369 (Oxford Univ. Press, 2014). – Chapter 13 – Pathogenic mechanisms

Klapstein, G. J., Fisher, R. S., Zanjani, H., Cepeda, C., Jokel, E. S., Chesselet, M., & Levine,

M. S. (2001). Electrophysiological and morphological changes in striatal spiny neurons in R6/2 Huntington's Disease transgenic mice. *Journal of Neurophysiology, 86*(6), 2667-2677. doi:10.1152/jn.2001.86.6.2667

Leblang, C. J., Medalla, M., Nicoletti, N. W., Hays, E. C., Zhao, J., Shattuck, J., . . .

Luebke, J. I. (2020). Reduction of the RNA Binding Protein TIA1 Exacerbates Neuroinflammation in Tauopathy. *Frontiers in Neuroscience, 14*. doi:10.3389/fnins.2020.00285

Levey, A. I., Hersch, S. M., Rye, D. B., Sunahara, R. K., Niznik, H. B., Kitt, C. A., . . .

Ciliax, B.

J. (1993). Localization of d1 and d2 dopamine receptors in brain with subtype specific antibodies. *Proceedings of the National Academy of Sciences, 90*(19), 8861-8865. doi:10.1073/pnas.90.19.8861

Ludvigson, A. E., Luebke, J. I., Lewis, J., & Peters, A. (2011). Structural abnormalities in the cortex of the rTg4510 mouse model of tauopathy: A light and electron microscopy study. *Brain Structure and Function, 216*(1), 31-42. doi:10.1007/s00429-010-0295-4

Mangiarini, L., Sathasivam, K., Seller, M., Cozens, B., Harper, A., Hetherington, C., . . .

Bates, G.P. (1996). Exon 1 of the HD gene with an Expanded CAG repeat is sufficient to cause a progressive neurological phenotype in transgenic mice. *Cell,*

*87*(3), 493-506. doi:10.1016/s0092-8674(00)81369-0

Medalla, M., & Barbas, H. Synapses with inhibitory neurons differentiate anterior cingulate from dorsolateral prefrontal pathways associated with cognitive control. (2009) *Neuron 61*(4), 609-620. doi:10.1016/j.neuron.2009.01.006. PMID: 19249280; PMCID: PMC2804928.

Menalled, L. B., Kudwa, A. E., Miller, S., Fitzpatrick, J., Watson-Johnson, J., Keating, N., . . . Howland, D. (2012). Comprehensive behavioral and molecular characterization of a new knock-in mouse model of huntington's disease: Zq175. *PLoS ONE, 7*(12). doi:10.1371/journal.pone.0049838

Menalled, L. B., Sison, J. D., Dragatsis, I., Zeitlin, S., & Chesselet, M. (2003). Time course of early motor and neuropathological anomalies in a Knock-in mouse model of Huntington's disease with 140 CAG repeats. *The Journal of Comparative Neurology, 465*(1), 11-26. doi:10.1002/cne.10776

Monte, S. M., Vonsattel, J., & Richardson, E. P. (1988). Morphometric Demonstration of Atrophic Changes in the Cerebral Cortex, White Matter, and Neostriatum in Huntington's Disease. *Journal of Neuropathology & Experimental Neurology, 47*(5), 516-525. doi:10.1097/00005072-198809000-00003

Moss, J., & Bolam, J. P. (2008). A dopaminergic axon lattice in the striatum and its relationship with cortical and thalamic terminals. *Journal of Neuroscience, 28*(44), 11221-11230. doi:10.1523/jneurosci.2780-08.2008

National Institute of Neurological Disorders and Stroke (NINDS). (1998). *Huntington's disease: Hope through research*. Bethesda, MD

National Research Council (US) Committee for the Update of the Guide for the Care and Use of Laboratory Animals. (2011). *Guide for the Care and Use of Laboratory Animals*. (8th ed.). National Academies Press (US).

Negi, R. S., Manchanda, K. L., & Sanga, S. (2014). Imaging of Huntington's disease. *Medical journal, Armed Forces India*, *70*(4), 386–388. doi:10.1016/j.mjafi.2012.08.002

Papoutsi, M., Labuschagne, I., Tabrizi, S. J., & Stout, J. C. (2014). The cognitive burden in Huntington's disease: Pathology, phenotype, and mechanisms of compensation. *Movement Disorders, 29*(5), 673-683. doi:10.1002/mds.25864

Parievsky, A., Moore, C., Kamdjou, T., Cepeda, C., Meshul, C. K., & Levine, M. S. (2017). Differential electrophysiological and morphological alterations of thalamostriatal and corticostriatal projections in the R6/2 mouse model of Huntington's disease. *Neurobiology of Disease*, *108*, 29–44. https://doi.org/10.1016/j.nbd.2017.07.020

Peters, A., Palay, S., & Webster, H. (1991). The fine structure of the nervous system. New York: Oxford UP.

Peters, A., Sethares, C., & Luebke, J. (2008). Synapses are lost during aging in the primate prefrontal cortex. *Neuroscience, 152*(4), 970981. doi:10.1016/j.neuroscience.2007.07.014

Piggott, M., Marshall, E., Thomas, N., Lloyd, S., Court, J., Jaros, E., . . . Perry, E. (1999). Dopaminergic activities in the human striatum: Rostrocaudal gradients of uptake sites and of d1 and d2 but not of d3 receptor binding or dopamine.

*Neuroscience, 90*(2), 433-445. doi:10.1016/s0306-4522(98)00465-5

Pouladi, M. A., Stanek, L. M., Xie, Y., Franciosi, S., Southwell, A. L., Deng, Y., . . . Hayden,

M. R. (2012). Marked differences in neurochemistry and aggregates despite similar behavioural and neuropathological features of Huntington disease in the full-length BACHD and YAC128 mice. *Human Molecular Genetics, 21*(10), 2219 2232. doi:10.1093/hmg/dds037

Pringsheim, T., Wiltshire, K., Day, L., Dykeman, J., Steeves, T., & Jette, N. (2012). The incidence and prevalence of Huntington's disease: A systematic review and meta analysis. *Movement Disorders, 27*(9), 1083-1091. doi:10.1002/mds.25075

Reiner, A., Dragatsis, I., & Dietrich, P. (2011). Genetics and Neuropathology of Huntington's Disease. In *Pathophysiology, pharmacology, and biochemistry of dyskinesia* (Vol. 98, pp. 325-372). New York, New York: Academic Press. doi:10.1016/B978-0-12-387003-2.00014-8

Rocher, A. B., Gubellini, P., Merienne, N., Boussicault, L., Petit, F., Gipchtein, P., . . . Bonvento, G. (2016). Synaptic scaling up in medium spiny neurons of Aged BACHD Mice: A Slow-progression model of Huntington's disease. *Neurobiology of Disease, 86*, 131-139. doi:10.1016/j.nbd.2015.10.016

Schneider, C. A., Rasband, W. S., & Eliceiri, K. W. (2012). NIH Image to ImageJ: 25 years of image analysis. *Nature Methods*, *9*(7), 671-675.

Sidman, R. L., Angevine, J. B., & Pierce, E. T. (1971). *Atlas of the Mouse Brain and Spinal Cord*. Cambridge, MA: Harvard University Press.

Song, W., Chen, J., Petrilli, A. *et al*. (2011). Mutant huntingtin binds the mitochondrial fission GTPase dynamin-related protein-1 and increases its enzymatic activity. *Nature Medicine 17*, 377–382 (2011). https://doi.org/10.1038/nm.2313

Speer, M., Bhanji, J., & Delgado, M. (2014). Savoring the Past: Positive Memories Evoke Value Representations in the Striatum. *Neuron, 84*(4), 847-856. doi:10.1016/j.neuron.2014.0-9.028

Stauffer, W., Sheng, H., & Lim, H. N. (2018). EzColocalization: An ImageJ plugin for visualizing and measuring colocalization in cells and organisms. *Scientific reports*, *8*(1)15764. doi:10.1038/s41598-018-33592-8. PMID: 30361629; PMCID: PMC6202351.

Steiner, H., & Gerfen, C. R. (1998). Role of dynorphin and enkephalin in the regulation of striatal output pathways and behavior. *Experimental Brain Research, 123*(1-2), 60-76. doi:10.1007/s002210050545

Stocco, A., Lebiere, C., & Anderson, J. R. (2010). Conditional routing of information to the cortex: A model of the basal ganglia's role in cognitive coordination. *Psychological Review, 117*(2), 541-574. doi:10.1037/a0019077

Sugars, K.L., & Rubinsztein, D.C. (2003) Transcriptional abnormalities in Huntington disease. *Trends in Genetics 19*: 233–238

Swami, M., Hendricks, A. E., Gillis, T., Massood, T., Mysore, J., Myers, R. H., &

Wheeler, V. C. (2009). Somatic expansion of the Huntington's disease CAG repeat in the brain is associated with an earlier age of disease onset. *Human molecular genetics*, *18*(16), 3039–3047. doi:10.1093/hmg/ddp242

Sathasivam, K., Neueder, A., Gipson, T. A., Landles, C., Benjamin, A. C., Bondulich, M. K., Smith, D. L., Faull, R. L., Roos, R. A., Howland, D., Detloff, P. J., Housman, D. E., & Bates, G. P. (2013). Aberrant splicing of HTT generates the pathogenic exon 1 protein in Huntington disease. *Proceedings of the National Academy of Sciences of the United States of America*, *110*(6), 2366–2370. doi:h10.1073/pnas.1221891110

Trushina, E., Dyer, R. B., Badger, J. D., Ure, D., . . . McMurray, C. T. (2004). Mutant huntingtin impairs axonal trafficking in mammalian neurons in vivo and in vitro. *Molecular and Cellular Biology, 24*(18), 8195-8209. doi:10.1128/mcb.24.18.8195 8209.2004

US Department of Health and Human Services. (2015). *Public Health Service Policy on Humane Care and Use of Laboratory Animals*. Office of Laboratory Animal Welfare (OLAW)

Vonsattel, J. P., & DiFiglia, M. (1998). Huntington Disease. *Journal of Neuropathology and Experimental Neurology*, *57*, 369–384. doi:10.1097/00005072 19980500000001

Wang, J., & Barbas, H. Specificity of Primate Amygdalar Pathways to Hippocampus. (2018). *Journal of Neuroscience, 38*(47), 10019-10041. doi:10.1523/JNEUROSCI.1267-18-2018

Weeks, R.A., Piccini, P., Harding, A.E. and Brooks, D.J. (1996), Striatal D1 and D2 dopamine receptor loss in asymptomatic mutation carriers of Huntington's disease. *Annals of Neurology*, 40:49-54. doi:10.1002/ana.410400110

Zuccato, C., & Cattaneo, E. (2014). Normal Function of Huntingtin. *Oxford Medicine Online*. doi:10.1093/med/9780199929146.003.0011

**CURRICULUM VITAE**